ANALYTICAL LINEARIZATION OF ROTOR SIMULATION IN GROUND EFFECT USING A COUPLED PANEL AND VISCOUS VORTEX PARTICLE METHOD IN STATE-SPACE FORM

Hussien A. A. H. Hussien
Ph.D. Candidate
Department of Aerospace Engineering
University of Maryland
College Park, Maryland, U.S.A.

Umberto Saetti
Assistant Professor
Department of Aerospace Engineering
University of Maryland
College Park, Maryland, U.S.A.

ABSTRACT

This study extends previous work on the state-space formulation and analytical linearization of viscous vortex particle methods by incorporating ground effect into rotary-wing simulations. The aerodynamic solver couples a panel method for modeling blade surfaces and near-wake dynamics with a Viscous Vortex Particle Method (VVPM) for capturing the far-wake. Ground effect is modeled using the method of images. The combined formulation is expressed as a system of Ordinary Differential Equations (ODEs), resulting in a Non-Linear Time-Periodic (NLTP) system in first-order form. Two linearization techniques are applied to this NLTP system: a conventional finite-difference approach and an analytical linearization scheme extended to include ground influence. Harmonic decomposition is then used to convert the Linear Time-Periodic (LTP) model into a higher-order Linear Time-Invariant (LTI) system, enabling the development of a reduced-order linear model suitable for real-time analysis and control. The simulation model is implemented in MATLAB® and applied to a utility-scale helicopter rotor blade. Validation is performed against experimental and high-fidelity numerical results for In-Ground-Effect (IGE) conditions. The linearized models are shown to closely replicate the nonlinear system dynamics across time and frequency domains. Furthermore, the analytical linearization offers a substantial computational advantage over finite-difference methods, with an efficiency gain on the order of O(n^2). This simulation model enables accurate and efficient modeling of aerodynamic effects in rotary-wing applications, including ground effect interactions.

INTRODUCTION

Modern rotorcraft configurations, especially those envisioned for Future Vertical Lift (FVL) and Urban Air Mobility (UAM), feature multiple rotors, significant levels of aerodynamic interactions, and variable-speed rotors. Modeling these complex phenomena requires aeromechanics models beyond the blade-element and finite-state inflow models typically used in flight dynamics simulations, thereby making real-time simulation elusive. In fact, most high-fidelity aeromechanics tools – such as grid-free methods (*e.g.*, free-wake and vortex particle methods) and Computational Fluid Dynamics (CFD) solvers (Refs. 1, 2) – remain computationally intensive and cannot achieve real-time performance unless massively parallelized. Moreover, these methods are not formulated in state-space form, which precludes their linearization alongside the flight mechanics for use in stability analysis and flight control design.

Several notable simulation models have integrated advanced wake modeling capabilities in real time. GenHel employed the CHARM Wake Module to model main rotor inflow (Ref. 3), later adopted in Navy training environments (Ref. 4) and even adapted to eVTOL applications (Ref. 5). Similarly, FLIGHTLAB has incorporated viscous vortex particle methods (VVPM) for wake-blade interaction modeling in both helicopters and eVTOLs (Refs. 6, 7). While these platforms have significantly advanced rotorcraft simulation, their underlying numerical approaches are not structured to support systematic linearization or reduced-order model extraction.

To overcome these limitations, recent work has focused on formulating rotor wake models directly in state-space form. A notable example is the work of Celi (Ref. 8), who discretized the Maryland Free Wake Model (Refs. 9, 10) using the method of lines to convert it into a first-order system of ordinary differential equations. This formulation facilitates linearization and control design, but struggles with equilibrium definition due to the time-periodic nature of rotor wake dynamics. More recent implementations, such as the PSUHeloSim rotor model (Refs. 11, 12), incorporated a vortex lattice near-wake model and achieved linearization via time-periodic system theory. Still, these models are limited in resolving chordwise loading and are numerically unstable for modeling multi-rotor or rotor-wing interactions.

Meanwhile, Vortex Particle Methods (VPMs) have emerged as powerful mid-fidelity tools, offering a balance between accuracy and computational cost (Refs. 13, 14). Tools such as DUST (Ref. 15), FLIGHTLAB (Ref. 16), and other VPM-based solvers (Refs. 17–19) have demonstrated strong capabilities in modeling rotor interactions. However, their time-marching nature and lack of state-variable formulation preclude the extraction of linear models and make them unsuitable for capturing unstable dynamics, especially critical when modeling hover or transition phases.

To bridge this gap, a State-Space Panel and Vortex Particle Method (SSPVPM) was recently proposed (Ref. 20), enabling efficient linearization and promising real-time application potential. The solver was initially developed for fixed-wing configurations (Refs. 20,21), then extended to model rotary-wing systems (Refs. 22, 23), capturing the unsteady aerodynamics of rotor blades. Building on this, the Fast Multipole Method (FMM) was integrated to significantly accelerate the particle–particle interactions (Ref. 24), reducing computational cost and further improving the feasibility of real-time simulation. To enhance the physical realism of the method, viscous effects were incorporated using the Particle Strength Exchange (PSE) scheme, resulting in the State-Space Panel and *Viscous* Vortex Particle Method (SSPVVPM) (Ref. 25).

Building on this foundation, the present work has two main objectives. First, ground effects are incorporated into the SSPVVPM simulation model using the method of images (Ref. 26), enabling a more complete aerodynamic model for near-ground operations. Second, the SSPVVPM is analytically linearized to support reduced-order modeling and control design. The results from the nonlinear solver In-Ground Effect (IGE) are validated against experimental and computational work. The accuracy of the linearized model is validated against the full nonlinear dynamics, and its computational efficiency is compared against conventional perturbation-based linearization methods (Ref. 27).

The article begins by presenting the mathematical formulation of the coupled panel and viscous vortex particle method, expressed in Partial Differential Equation (PDE) form. The ground effect implementation using the method of images is then provided. Next, the spatial discretization process is detailed, converting the PDEs into Ordinary Differential Equations (ODEs). Two linearization schemes are used to linearize the enhanced solver: a conventional perturbation linearization scheme and an analytical linearization scheme. Furthermore, a reduced order model is introduced to the current simulation model. In the results section, the nonlinear solver is first validated against experimental data, followed by a comparison of the linear models with the nonlinear solver in both time and frequency domains. The study concludes with a thorough evaluation of the linear solver's computational efficiency.

COUPLED PANEL AND VISCOUS VORTEX PARTICLE METHODS

The simulation model employed in this work builds upon the state-space panel and viscous vortex particle method developed in Refs. 21, 23, with a key enhancement. Panels are used to model the surface of the blade as well as the near-wake region, while the far wake is represented using viscous vortex particles. A schematic of the overall model architecture is presented in Fig. 1.

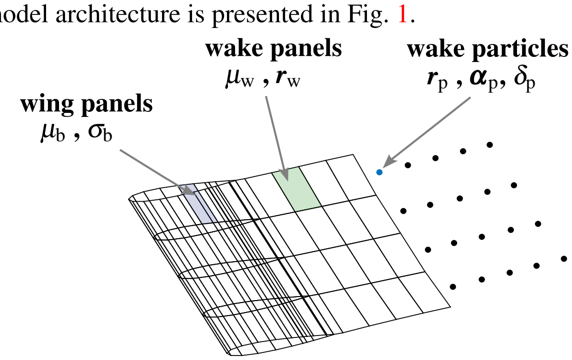

Figure 1: Simulation model schematic.

The main advancement over previous implementations, including Ref. 23, is the integration of ground effects through the method of images. This extension enables the simulation of the IGE conditions, thereby broadening the applicability of the solver to scenarios involving ground proximity.

PDE Formulation

The aerodynamic model follows a vorticity–velocity formulation based on Helmholtz's decomposition and a Lagrangian description of vorticity transport. Incompressibility reduces the continuity equation to the Laplace equation for the potential function:

$$\Delta\varphi = 0 \tag{1}$$

which is solved using Morino's method (Ref. 28) to obtain surface pressures. The unsteady evolution of vorticity is governed by the Lagrangian form of the incompressible Navier–Stokes equations:

$$\frac{D\boldsymbol{\omega}}{Dt} = (\boldsymbol{\omega}\cdot\nabla)\boldsymbol{u} + \nu_\infty \nabla^2 \boldsymbol{\omega} \tag{2}$$

where ν_∞ is the kinematic viscosity and $D\boldsymbol{\omega}/Dt$ is the material derivative.

Blade and Wake Panel Intensity To solve the Laplace equation in Eq. (1), Morino's method (Ref. 28) is applied using a Green's function formulation. The surface of the blade is discretized into panels with uniform source σ_b and uniform doublet μ_b strengths. The sources are used to enforce the non-penetration condition on the blade surface:

$$\sigma_\mathrm{b} = -\hat{\boldsymbol{n}}\cdot(\boldsymbol{u}_\mathrm{b} - \boldsymbol{U}_\infty - \boldsymbol{u}_\psi) \tag{3}$$

where $\hat{\boldsymbol{n}}$ represents the normal vectors of the blade panels, $\boldsymbol{u}_\mathrm{b}$ is the body velocity, $\boldsymbol{U}_\infty$ denotes the free-stream velocity, and $\boldsymbol{u}_\psi$ is the velocity induced by the vortex particles.

The near wake is discretized into panels with doublet intensities μ_w, while the rotational flow is captured by particles of strength α_p.

The discrete form of the Laplace problem is (Ref. 29):

$$\boldsymbol{A}_\mathrm{b}\boldsymbol{\mu}_\mathrm{b} + \boldsymbol{A}_\mathrm{w}^\mathrm{TE}\boldsymbol{\mu}_\mathrm{w}^\mathrm{TE} + \boldsymbol{A}_\mathrm{w}\boldsymbol{\mu}_\mathrm{w} + \boldsymbol{B}_\mathrm{b}\boldsymbol{\sigma}_\mathrm{b} = \boldsymbol{0} \tag{4}$$

where matrices' dimensions are defined by the number of blades and near wake panels.

Three additional boundary conditions are incorporated: (i) the Kutta condition at the trailing edge (Ref. 28), (ii) a conversion relation between wake panel and vortex particle strengths (Ref. 23), and (iii) an advection update for wake panel strengths (Ref. 8):

$$\boldsymbol{K}_5\boldsymbol{\mu}_\mathrm{b} = \boldsymbol{\mu}_\mathrm{w}^\mathrm{TE} \tag{5a}$$

$$\boldsymbol{K}_6\boldsymbol{\mu}_\mathrm{w} = \boldsymbol{\alpha}_\mathrm{p} \tag{5b}$$

$$\boldsymbol{K}_7\boldsymbol{\mu}_\mathrm{w} + \boldsymbol{K}_8\boldsymbol{\mu}_\mathrm{w}^\mathrm{TE} = \boldsymbol{\mu}_\mathrm{w}^{t+1} \tag{5c}$$

By combining Eqs. (3), (4), and (5), the surface doublet strengths can be expressed in terms of wake quantities and body motion:

$$\boldsymbol{\mu}_\mathrm{b} = -\boldsymbol{K}_9\left[\boldsymbol{K}_3\boldsymbol{\mu}_\mathrm{w} + \boldsymbol{B}'(\boldsymbol{u}_\psi - \boldsymbol{u}_\mathrm{b} + \boldsymbol{U}_\infty)\right] \tag{6}$$

where the auxiliary matrices are defined as:

$$\boldsymbol{K}_9 = \left(\boldsymbol{A}_\mathrm{b} + \boldsymbol{A}_\mathrm{w}^\mathrm{TE}\boldsymbol{K}_5\right)^{-1} \tag{7a}$$

$$\boldsymbol{K}_3 = \boldsymbol{A}_\mathrm{w} \tag{7b}$$

$$\boldsymbol{B}' = \boldsymbol{B}_\mathrm{b}\boldsymbol{N} \tag{7c}$$

and $\boldsymbol{N}$ contains the unit normal vectors of the body panels.

Vortex Particle Intensity The vorticity field is discretized using N_p vortex particles following Winckelmans' formulation (Ref. 13):

$$\boldsymbol{\omega}(\boldsymbol{r},t) = \sum_{i=1}^{N_\mathrm{p}} \boldsymbol{\alpha}_\mathrm{p}^i(t)\,\delta\left(\boldsymbol{r}_\mathrm{p}^i(t) - \boldsymbol{r}\right) \tag{8}$$

where $\boldsymbol{r}_\mathrm{p}^i$ and $\boldsymbol{\alpha}_\mathrm{p}^i$ denote the position and strength of the i^th particle, respectively. The induced velocity field by the vortex particles is defined as (Ref. 30):

$$\begin{aligned}\boldsymbol{u}_\psi(\boldsymbol{r},t) &= -\frac{1}{4\pi}\sum_{i=1}^{N_\mathrm{p}} c_i\left[\left(\boldsymbol{r}_\mathrm{p}^i - \boldsymbol{r}\right)\times\boldsymbol{\alpha}_\mathrm{p}^i(t)\right] \\ &= [\boldsymbol{K}_\psi(\boldsymbol{r}_\mathrm{p},\boldsymbol{r})\times]\boldsymbol{\alpha}_\mathrm{p}(t) = \boldsymbol{K}_4(\boldsymbol{r}_\mathrm{p},\boldsymbol{r})\,\boldsymbol{\alpha}_\mathrm{p}(t)\end{aligned} \tag{9}$$

where c_i and $\boldsymbol{K}_\psi$ are regularization functions defined in Ref. 23.

Method of Lines

The Method of Lines is used to transform the wake panel and vortex particle aerodynamics described above from PDE to ODE form (Refs. 9,10,24,31). This method uses a spatial discretization matrix, also known as a shifting matrix, to transform wake dynamics into a state-space form as discussed in 8,31. The motion of a generic collocation point follows:

$$\frac{D\boldsymbol{r}}{Dt} = \boldsymbol{v}_\mathrm{ind} \tag{10}$$

where D/Dt denotes the total derivative and $\boldsymbol{v}_\mathrm{ind}$ is the induced velocity, composed of contributions from particles and panels (Ref. 22). Applying the chain rule, the governing PDE becomes:

$$\frac{\partial\boldsymbol{r}}{\partial t} + \frac{\partial\boldsymbol{r}}{\partial\boldsymbol{x}} = \boldsymbol{v}_\mathrm{ind} \tag{11}$$

with $\boldsymbol{x}$ denoting spatial location. Discretizing the spatial domain yields a system of ODEs:

$$\frac{\partial\boldsymbol{r}}{\partial t} = \dot{\boldsymbol{r}} = \boldsymbol{A}\boldsymbol{r} + \boldsymbol{v}_\mathrm{ind} \tag{12}$$

where $\boldsymbol{A}$ is the spatial discretization matrix. Different approximations of $\boldsymbol{A}$ are provided in Ref. 8.

State-Space Formulation

The coupled panel and viscous vortex particle dynamics are formulated as a Non-Linear, Time-Periodic (NLTP) system of first-order ODEs:

$$\dot{\boldsymbol{x}} = \boldsymbol{f}(\boldsymbol{x},\boldsymbol{u},t) \tag{13a}$$

$$\boldsymbol{y} = \boldsymbol{g}(\boldsymbol{x},\boldsymbol{u},t) \tag{13b}$$

where $\boldsymbol{x} \in \mathbb{R}^n$, $\boldsymbol{u} \in \mathbb{R}^m$, and $\boldsymbol{y} \in \mathbb{R}^l$ represent the state, control input, and output vectors, respectively. The functions $\boldsymbol{f}$ and $\boldsymbol{g}$ are periodic in time with period $T_\mathrm{p} = 2\pi/\Omega$, where Ω is the rotor speed:

$$\boldsymbol{f}(\cdot,t) = \boldsymbol{f}(\cdot,t+T_\mathrm{p}) \tag{14a}$$
$$\boldsymbol{g}(\cdot,t) = \boldsymbol{g}(\cdot,t+T_\mathrm{p}) \tag{14b}$$

The state vector includes the wake panel intensities $\boldsymbol{\mu}_\mathrm{w}$, the vortex particle intensities $\boldsymbol{\alpha}_\mathrm{p}$, the positions of the wake panels $\boldsymbol{r}_\mathrm{w}$, the positions of the vortex particles $\boldsymbol{r}_\mathrm{p}$, the wing panel intensities $\boldsymbol{\mu}_\mathrm{b}$, and the vortex particle core radii $\boldsymbol{\delta}_\mathrm{p}$:

$$\boldsymbol{x}^\mathrm{T} = \left\{\boldsymbol{\mu}_\mathrm{w}^\mathrm{T} \quad \boldsymbol{\alpha}_\mathrm{p}^\mathrm{T} \quad \boldsymbol{r}_\mathrm{w}^\mathrm{T} \quad \boldsymbol{r}_\mathrm{p}^\mathrm{T} \quad \boldsymbol{\mu}_\mathrm{b}^\mathrm{T} \quad \boldsymbol{\delta}_\mathrm{p}^\mathrm{T}\right\} \tag{15}$$

The inputs are the blade pitch controls:

$$\boldsymbol{u}^\mathrm{T} = \left\{\theta_0 \quad \theta_{1\mathrm{c}} \quad \theta_{1\mathrm{s}}\right\} \tag{16}$$

and the outputs include pressure distribution and aerodynamic loads:

$$\boldsymbol{y}^\mathrm{T} = \left\{\boldsymbol{p}^\mathrm{T} \quad \boldsymbol{F}_\mathrm{a}^\mathrm{T}\right\} \tag{17}$$

Wake Panel Intensities The evolution of the wake doublet intensities can be computed using Eqs. (5), (6), and (9):

$$\dot{\boldsymbol{\mu}}_\mathrm{w} = (\boldsymbol{W}_1 - \boldsymbol{W}_2\boldsymbol{K}_5\boldsymbol{K}_9\boldsymbol{K}_3)\boldsymbol{\mu}_\mathrm{w} - \boldsymbol{W}_2\boldsymbol{K}_5\boldsymbol{K}_9\boldsymbol{B}'\boldsymbol{K}_4\boldsymbol{\alpha}_\mathrm{p} + \boldsymbol{W}_2\boldsymbol{K}_5\boldsymbol{K}_9\boldsymbol{B}'(\boldsymbol{u}_\mathrm{b} - \boldsymbol{U}_\infty) \tag{18}$$

Details can be found in Ref. 23.

Wake Particle Intensities The vorticity fields are described using the transpose method (Ref. 30):

$$\dot{\boldsymbol{\alpha}}_\mathrm{p}^* = \sum_j^{N_p}\left[-\frac{1}{4\pi}\left[c_j\,\boldsymbol{\alpha}_\mathrm{p}^j \times \boldsymbol{\alpha}_\mathrm{p} + d_j\,\Delta\boldsymbol{r}_j(\Delta\boldsymbol{r}_j\cdot\boldsymbol{\alpha}_\mathrm{p}^j\times\boldsymbol{\alpha}_\mathrm{p})\right] - \nu_\infty\eta_\delta(\boldsymbol{r}_\mathrm{p} - \boldsymbol{r}_\mathrm{p}^j)[vol_\mathrm{p}\,\boldsymbol{\alpha}_\mathrm{p}^j - vol_\mathrm{p}^j\,\boldsymbol{\alpha}_\mathrm{p}]\right] \tag{19}$$

In this formula, the viscous effects are implemented using the PSE method (Ref. 32). Different terms in Eq. (19) can be found in Ref. 25.

To enhance hover stability, Eq. (19) is further refined by integrating the modified vortex particle method introduced by Alvarez (Ref. 19):

$$\dot{\boldsymbol{\alpha}}_\mathrm{p} = \dot{\boldsymbol{\alpha}}_\mathrm{p}^* - \frac{g+f}{1/3+f}\left[\dot{\boldsymbol{\alpha}}_\mathrm{p}^*\cdot\hat{\boldsymbol{\alpha}}_\mathrm{p}\right]\hat{\boldsymbol{\alpha}}_\mathrm{p} \tag{20}$$

In this context, $\hat{\boldsymbol{\alpha}}_\mathrm{p}$ represents the normalized particle strength vector, calculated as $\boldsymbol{\alpha}_\mathrm{p}/\|\boldsymbol{\alpha}_\mathrm{p}\|$, while f and g are constants determined from a specific application of conservation principles (Ref. 19).

Position of Wake Panel Nodes and Particles The induced velocity, $\boldsymbol{v}_\mathrm{ind}$, is determined using the Biot-Savart law, as outlined in Refs. 29, 31. At any point $\boldsymbol{r}$, the induced velocity can be expressed as:

$$\boldsymbol{v}_\mathrm{ind} = \boldsymbol{v}_\mathrm{b}^\sigma + \boldsymbol{v}_\mathrm{b}^\mu + \boldsymbol{v}_\mathrm{w}^\mu + \boldsymbol{v}_\mathrm{p} \tag{21}$$

where each term represents a specific contribution:

$$\boldsymbol{v}_\mathrm{b}^\sigma = \boldsymbol{v}_\mathrm{b}^\sigma(\boldsymbol{\sigma}_\mathrm{b},\boldsymbol{r}) \tag{22a}$$
$$\boldsymbol{v}_\mathrm{b}^\mu = \boldsymbol{v}_\mathrm{b}^\mu(\boldsymbol{\mu}_\mathrm{b},\boldsymbol{r}) \tag{22b}$$
$$\boldsymbol{v}_\mathrm{w}^\mu = \boldsymbol{v}_\mathrm{w}^\mu(\boldsymbol{\mu}_\mathrm{w},\boldsymbol{r}_\mathrm{w},\boldsymbol{r}) \tag{22c}$$
$$\boldsymbol{v}_\mathrm{p} = \boldsymbol{v}_\mathrm{p}(\boldsymbol{\alpha}_\mathrm{p},\boldsymbol{r}_\mathrm{p},\boldsymbol{\delta}_\mathrm{p},\boldsymbol{r}) \tag{22d}$$

where the definitions of these terms can be found in Ref. 23.

Blade Panel Intensities The dynamics of the wing doublet intensities are determined using Eq. (6), as outlined below:

$$\dot{\boldsymbol{\mu}}_\mathrm{b} = \frac{1}{\tau}\left[-\boldsymbol{K}_9\boldsymbol{K}_3\boldsymbol{\mu}_\mathrm{w} - \boldsymbol{K}_9\boldsymbol{B}'\boldsymbol{K}_4\boldsymbol{\alpha}_\mathrm{p} + \boldsymbol{K}_9\boldsymbol{B}'(\boldsymbol{u}_\mathrm{b} - \boldsymbol{U}_\infty) - \boldsymbol{\mu}_\mathrm{b}\right] \tag{23}$$

where τ is the time constant of a first-order filter.

Wake Particle Core Radii The time-dependent behavior of the wake particle core radii, $\boldsymbol{\delta}_\mathrm{p}$, is governed by the equation outlined in Ref. 19:

$$\dot{\boldsymbol{\delta}}_\mathrm{p} = -\frac{g+f}{1+3f}\frac{\boldsymbol{\delta}_\mathrm{p}}{\|\boldsymbol{\alpha}_\mathrm{p}\|}\left[\dot{\boldsymbol{\alpha}}_\mathrm{p}^*\cdot\hat{\boldsymbol{\alpha}}_\mathrm{p}\right] \tag{24}$$

Aerodynamic Loads and Surface Pressure To calculate the pressure at the center of the blade panels while accounting for compressibility effects, the Prandtl-Glauert compressibility correction (Ref. 33) is applied, using the unsteady Bernoulli theorem (Ref. 34):

$$\boldsymbol{p} = p_\infty + \rho_\infty\left[\frac{1}{2}\|\boldsymbol{U}_\infty\|^2 - \frac{1}{2}\|\boldsymbol{u}_\mathrm{surf}\|^2 + \boldsymbol{u}_\mathrm{b}\cdot\left(\nabla\boldsymbol{\mu}_\mathrm{b} + \boldsymbol{u}_\psi^b\right) + \dot{\boldsymbol{\mu}}_\mathrm{b}\right]/\sqrt{1-\boldsymbol{M}^2} \tag{25}$$

where $\boldsymbol{M}$ are the local Mach numbers computed at the centers of the blade panels and:

$$\boldsymbol{u}_\mathrm{surf} = \boldsymbol{U}_\infty + \nabla\boldsymbol{\mu}_\mathrm{b} + \boldsymbol{u}_\psi^b \tag{26}$$

In this equation, $\nabla\boldsymbol{\mu}_\mathrm{b}$ is determined using the Constrained Hermite Taylor Series Least Squares (CHTLS) method (Ref. 35).

When the pressure distribution is obtained, the aerodynamic loads on the blade are computed as follows:

$$\boldsymbol{F}_{\mathrm{a}} = \sum_{i}^{N_{\mathrm{b}}} p_i A_i \boldsymbol{n}_i = \hat{\boldsymbol{A}} \boldsymbol{p} \tag{27}$$

where A_i represents the surface area of the i^{th} wing panel, $\boldsymbol{n}_i$ is the normal vector associated with the i^{th} panel, and $\hat{\boldsymbol{A}}$ is a matrix containing the area vectors of the blade panels.

Summary of State-Space Model A summary of the differential equations is provided below:

$$\begin{aligned} \dot{\boldsymbol{\mu}}_{\mathrm{w}} = {} & (\boldsymbol{W}_1 - \boldsymbol{W}_2\boldsymbol{K}_5\boldsymbol{K}_9\boldsymbol{K}_3)\boldsymbol{\mu}_{\mathrm{w}} - \\ & \boldsymbol{W}_2\boldsymbol{K}_5\boldsymbol{K}_9\boldsymbol{B}'\boldsymbol{K}_4\boldsymbol{\alpha}_{\mathrm{p}} + \boldsymbol{W}_2\boldsymbol{K}_5\boldsymbol{K}_9\boldsymbol{B}'(\boldsymbol{u}_{\mathrm{b}} - \boldsymbol{U}_\infty) \end{aligned} \tag{28a}$$

$$\dot{\boldsymbol{\alpha}}_{\mathrm{p}} = -\boldsymbol{A}^{\alpha_{\mathrm{p}}}\,\boldsymbol{\alpha}_{\mathrm{p}} + \dot{\boldsymbol{\alpha}}_{\mathrm{p}}^{*} - \frac{g + f}{1/3 + f}\left[\dot{\boldsymbol{\alpha}}_{\mathrm{p}}^{*} \cdot \hat{\boldsymbol{\alpha}}_{\mathrm{p}}\right]\hat{\boldsymbol{\alpha}}_{\mathrm{p}} \tag{28b}$$

$$\dot{\boldsymbol{r}}_{\mathrm{w}} = -\boldsymbol{A}^{r_{\mathrm{w}}}\boldsymbol{r}_{\mathrm{w}} + \boldsymbol{v}_{\mathrm{ind}}(\boldsymbol{r}_{\mathrm{w}}, \boldsymbol{r}_{\mathrm{p}}, \boldsymbol{\alpha}_{\mathrm{p}}, \boldsymbol{\mu}_{\mathrm{w}}, \boldsymbol{\mu}_{\mathrm{b}}, \boldsymbol{\delta}_{\mathrm{p}}) \tag{28c}$$

$$\dot{\boldsymbol{r}}_{\mathrm{p}} = -\boldsymbol{A}^{r_{\mathrm{p}}}\boldsymbol{r}_{\mathrm{p}} + \boldsymbol{v}_{\mathrm{ind}}(\boldsymbol{r}_{\mathrm{w}}, \boldsymbol{r}_{\mathrm{p}}, \boldsymbol{\alpha}_{\mathrm{p}}, \boldsymbol{\mu}_{\mathrm{w}}, \boldsymbol{\mu}_{\mathrm{b}}, \boldsymbol{\delta}_{\mathrm{p}}) \tag{28d}$$

$$\begin{aligned} \dot{\boldsymbol{\mu}}_{\mathrm{b}} = {} & \frac{1}{\tau}\Big[-\boldsymbol{K}_9\boldsymbol{K}_3\boldsymbol{\mu}_{\mathrm{w}} - \boldsymbol{K}_9\boldsymbol{B}'\boldsymbol{K}_4\boldsymbol{\alpha}_{\mathrm{p}} + \\ & \boldsymbol{K}_9\boldsymbol{B}'(\boldsymbol{u}_{\mathrm{b}} - \boldsymbol{U}_\infty) - \boldsymbol{\mu}_{\mathrm{b}}\Big] \end{aligned} \tag{28e}$$

$$\dot{\boldsymbol{\delta}}_{\mathrm{p}} = -\boldsymbol{A}^{\delta_{\mathrm{p}}}\,\boldsymbol{\delta}_{\mathrm{p}} - \frac{g + f}{1 + 3f}\frac{\boldsymbol{\delta}_{\mathrm{p}}}{\|\boldsymbol{\alpha}_{\mathrm{p}}\|}\left[\dot{\boldsymbol{\alpha}}_{\mathrm{p}}^{*} \cdot \hat{\boldsymbol{\alpha}}_{\mathrm{p}}\right] \tag{28f}$$

And the output equations are:

$$\begin{aligned} \boldsymbol{p} = {} & p_\infty + \rho_\infty\Big[\frac{1}{2}\|\boldsymbol{U}_\infty\|^2 - \frac{1}{2}\|\boldsymbol{u}_{\mathrm{surf}}\|^2 + \\ & \boldsymbol{u}_{\mathrm{b}} \cdot \left(\nabla\boldsymbol{\mu}_{\mathrm{b}} + \boldsymbol{u}_{\psi}^{b}\right) + \dot{\boldsymbol{\mu}}_{\mathrm{b}}\Big] \Big/ \sqrt{1 - \boldsymbol{M}^2} \end{aligned} \tag{29a}$$

$$\boldsymbol{F}_{\mathrm{a}} = \hat{\boldsymbol{A}}\boldsymbol{p} \tag{29b}$$

Definitions of the parameters appearing in Eqs. (28) and (29) can be located in Ref. 23.

GROUND EFFECT

Overview

The following three main approaches have been adopted to model ground effect for rotorcraft.

Method of Images (MOI) The first method is the so-called Method of Images (MOI) (Refs. 26,36). This technique mirrors the entire rotor system, including the blades and their wake, about the ground plane. The induced velocity field generated by this image system is superimposed onto the 'real' flow field, thereby satisfying the non-penetration boundary condition at the ground plane (GP). This model ensures the vertical component of induced velocity v_z at the ground plane, $z = \text{GP}$, is zero, as the induced velocities from the wake and rotor and their images cancel out:

$$v_z^{\mathrm{tot}}(z = \text{GP}) = v_z^{\mathrm{main}}(z = \text{GP}) + v_z^{\mathrm{image}}(z = \text{GP}) = 0 \tag{30}$$

This implicitly satisfies the tangential boundary condition at the ground plane. MOI is attractive for its simplicity and low computational cost, and it performs well for cases involving infinite flat ground. However, it cannot easily accommodate finite, non-planar, or complicated surfaces.

Surface Singularity Method The second method is a surface singularity method, also described in Ref. 26. In this approach, the ground is modeled using a grid of panels, each endowed with a source singularity, σ^{GP}, of unknown strength. These singularities are solved for by enforcing flow tangency at discrete control points, typically located at the panel center. This results in a linear system of equations that can be solved to determine the singularity strengths. The total induced velocity at any point is defined as:

$$\boldsymbol{v}_{\mathrm{ind}}^{\mathrm{tot}} = \boldsymbol{U}_\infty + \boldsymbol{v}_{\mathrm{ind}} + \boldsymbol{v}_{\mathrm{ind}}^{\mathrm{GP}} \tag{31}$$

where $\boldsymbol{v}_{\mathrm{ind}}^{\mathrm{GP}}$ is the velocity induced by the ground plane panels. Mathematically, the boundary condition at a point $\boldsymbol{x}_i$ on the ground enforces:

$$\left(\boldsymbol{U}_\infty + \boldsymbol{v}_{\mathrm{ind}} + \boldsymbol{v}_{\mathrm{ind}}^{\mathrm{GP}}\right) \cdot \hat{\mathbf{n}} = \mathbf{0} \tag{32}$$

where $\hat{\mathbf{n}}$ is the unit normal vector at the control points of the ground plane panels. Now, reorganizing Eq. (32):

$$\boldsymbol{v}_{\mathrm{ind}}^{\mathrm{GP}} \cdot \hat{\mathbf{n}} = \boldsymbol{\Upsilon}\boldsymbol{\sigma}^{\mathrm{GP}} \cdot \hat{\mathbf{n}} = \boldsymbol{A}\,\boldsymbol{\sigma}^{\mathrm{GP}} = -\left(\boldsymbol{U}_\infty + \boldsymbol{v}_{\mathrm{ind}}\right) \cdot \hat{\mathbf{n}} \tag{33}$$

where $\boldsymbol{\Upsilon}$ matrix is based on the source-induced velocity governing equation (Ref. 29), only dependent on the geometric relation between the ground plane panels. Hence, it only needs to be computed once. This method provides more flexibility than MOI and allows for arbitrary ground geometries, but it still does not satisfy the no-slip condition.

Vortex Sheet Method A third and more advanced approach is the vortex sheet method (Ref. 37). This technique also discretizes the ground using panels, but instead of source singularities, each panel is assigned a vortex sheet, $\boldsymbol{\gamma}$. This method is capable of satisfying both the non-penetration as well as the no-slip boundary conditions, making it more physically accurate in the near-ground region where viscous effects and shear layers become important. To solve for the vortex sheet, two boundary conditions have to be satisfied at the control point of the ground plane panels:

$$\left(\boldsymbol{U}_\infty + \boldsymbol{v}_{\mathrm{ind}} + \boldsymbol{v}_{\mathrm{ind}}^{\mathrm{GP}}\right) \cdot \hat{\mathbf{n}} = 0 \tag{34a}$$

$$\left(\boldsymbol{U}_\infty + \boldsymbol{v}_{\mathrm{ind}} + \boldsymbol{v}_{\mathrm{ind}}^{\mathrm{GP}}\right) \cdot \hat{\mathbf{t}} = 0 \tag{34b}$$

where $\hat{\mathbf{t}}$ are the normal and tangential unit vectors on the ground surface.

In summary, these three approaches represent a trade-off between accuracy and computational efficiency. The method of images is straightforward and efficient, but limited to simple ground geometries. The surface singularity method adds flexibility and explicit representation. The vortex sheet method satisfies both non-penetration and no-slip conditions at the cost of increased computational and implementation complexity.

Implementation

In the present work, MOI is used to account for the ground effect. MOI models the ground effect by creating an image of the rotor below the ground plane, as shown in Fig. 2. This approach was first applied to ground effect problems by Knight and Hefner (Ref. 38) using a vortex cylinder model. It was later adopted in the works of Saberi and Maisel (Ref. 39), as well as Rossow (Ref. 40), as well as Leishman (Ref. 26).

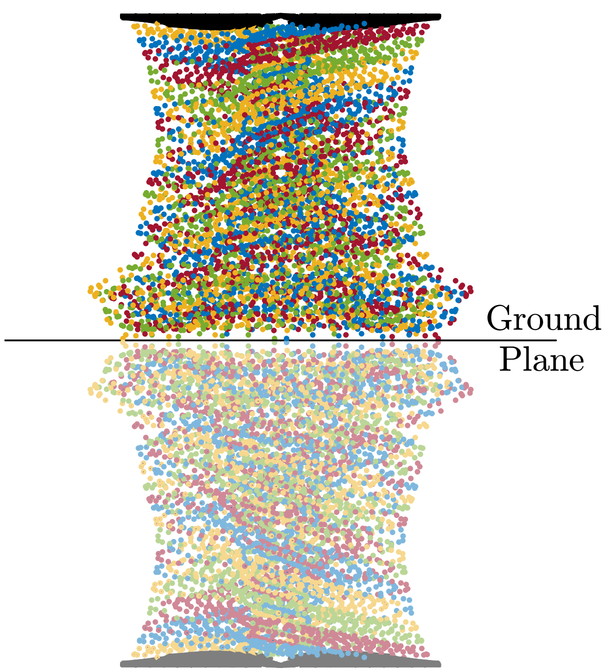

Figure 2: Method of Images illustration.

In the inertial frame, the wake and its image share identical x and y coordinates but have opposite z coordinates. The strengths of the image are of the opposite sign of the main domain. The states of the image are as follows:

$$\boldsymbol{\mu}_{\mathrm{w}}^{\mathrm{image}} = -\boldsymbol{\mu}_{\mathrm{w}} \tag{35a}$$

$$\boldsymbol{\alpha}_{\mathrm{p}} : (\boldsymbol{\alpha}_{\mathrm{p}}^{x}, \boldsymbol{\alpha}_{\mathrm{p}}^{y}, \boldsymbol{\alpha}_{\mathrm{p}}^{z})^{\mathrm{image}} = (-\boldsymbol{\alpha}_{\mathrm{p}}^{x}, -\boldsymbol{\alpha}_{\mathrm{p}}^{y}, \boldsymbol{\alpha}_{\mathrm{p}}^{z}) \tag{35b}$$

$$\boldsymbol{r}_{\mathrm{w}} \ : \ (\boldsymbol{x},\boldsymbol{y},\boldsymbol{z})_{\mathrm{w}}^{\mathrm{image}} = (\boldsymbol{x},\boldsymbol{y},-\boldsymbol{z})_{\mathrm{w}} \tag{35c}$$

$$\boldsymbol{r}_{\mathrm{p}} \ : \ (\boldsymbol{x},\boldsymbol{y},\boldsymbol{z})_{\mathrm{p}}^{\mathrm{image}} = (\boldsymbol{x},\boldsymbol{y},-\boldsymbol{z})_{\mathrm{p}} \tag{35d}$$

$$\boldsymbol{\mu}_{\mathrm{b}}^{\mathrm{image}} = -\boldsymbol{\mu}_{\mathrm{b}} \tag{35e}$$

$$\boldsymbol{\delta}_{\mathrm{p}}^{\mathrm{image}} = \boldsymbol{\delta}_{\mathrm{p}} \tag{35f}$$

When adding the image rotor to the free-vortex wake model, the solution algorithm is modified to account for both the above-ground rotor and wake and their image. Induced velocities at any collocation point are calculated by considering the influence of both systems (Eqs. (28c) and (28d)):

$$\dot{\boldsymbol{r}}_{\mathrm{w}}^{\mathrm{tot}} = \dot{\boldsymbol{r}}_{\mathrm{w}}^{\mathrm{main}} + \dot{\boldsymbol{r}}_{\mathrm{w}}^{\mathrm{image}} \tag{36a}$$

$$\dot{\boldsymbol{r}}_{\mathrm{p}}^{\mathrm{tot}} = \dot{\boldsymbol{r}}_{\mathrm{p}}^{\mathrm{main}} + \dot{\boldsymbol{r}}_{\mathrm{p}}^{\mathrm{image}} \tag{36b}$$

These are the only equations that need to be modified in Eqs. (28) and (29). The method of images is beneficial for two reasons: simplicity, as it creates symmetry about the ground plane and satisfies the boundary condition; and computational efficiency, as it avoids storing additional wake geometry data for the image, thereby saving memory.

LINEARIZATION

This section outlines the theoretical simulation model and implementation details for linearizing the coupled panel and wake dynamics using both numerical perturbation methods and a novel analytical approach.

Numerical Linearization Consider the non-linear time-invariant (NLTI) coupled panels and wake dynamics at equilibrium:

$$\dot{\bar{\boldsymbol{x}}} = \boldsymbol{f}\left(\bar{\boldsymbol{x}}, \bar{\boldsymbol{u}}\right) \tag{37a}$$

$$\bar{\boldsymbol{y}} = \boldsymbol{g}\left(\bar{\boldsymbol{x}}, \bar{\boldsymbol{u}}\right) \tag{37b}$$

where $\bar{\boldsymbol{x}} \in \mathscr{R}^n$, $\bar{\boldsymbol{u}} \in \mathscr{R}^m$, and $\bar{\boldsymbol{y}} \in \mathscr{R}^l$ are the trim state, control input, and output vectors such that the state dynamics $\dot{\bar{\boldsymbol{x}}}$ and output $\bar{\boldsymbol{y}}$ are constant. Using Taylor series expansion and by neglecting those terms with order higher than first, the linearized system can be written as:

$$\boldsymbol{\Delta}\dot{\boldsymbol{x}} = \boldsymbol{A}\boldsymbol{\Delta}\boldsymbol{x} + \boldsymbol{B}\boldsymbol{\Delta}\boldsymbol{u} \tag{38a}$$

$$\boldsymbol{\Delta}\boldsymbol{y} = \boldsymbol{C}\boldsymbol{\Delta}\boldsymbol{x} + \boldsymbol{D}\boldsymbol{\Delta}\boldsymbol{u} \tag{38b}$$

where:

$$\boldsymbol{A} = \frac{\partial \boldsymbol{f}(\boldsymbol{x},\boldsymbol{u})}{\partial \boldsymbol{x}}\bigg|_{\bar{\boldsymbol{x}},\bar{\boldsymbol{u}}} = \begin{bmatrix} \frac{\partial f_1(\boldsymbol{x},\boldsymbol{u})}{\partial x_1} & \cdots & \frac{\partial f_1(\boldsymbol{x},\boldsymbol{u})}{\partial x_n} \\ \vdots & \ddots & \vdots \\ \frac{\partial f_n(\boldsymbol{x},\boldsymbol{u})}{\partial x_1} & \cdots & \frac{\partial f_n(\boldsymbol{x},\boldsymbol{u})}{\partial x_n} \end{bmatrix}_{\bar{\boldsymbol{x}},\bar{\boldsymbol{u}}} \tag{39a}$$

$$\boldsymbol{B} = \frac{\partial \boldsymbol{f}(\boldsymbol{x},\boldsymbol{u})}{\partial \boldsymbol{u}}\bigg|_{\bar{\boldsymbol{x}},\bar{\boldsymbol{u}}} = \begin{bmatrix} \frac{\partial f_1(\boldsymbol{x},\boldsymbol{u})}{\partial u_1} & \cdots & \frac{\partial f_1(\boldsymbol{x},\boldsymbol{u})}{\partial u_m} \\ \vdots & \ddots & \vdots \\ \frac{\partial f_n(\boldsymbol{x},\boldsymbol{u})}{\partial u_1} & \cdots & \frac{\partial f_n(\boldsymbol{x},\boldsymbol{u})}{\partial u_m} \end{bmatrix}_{\bar{\boldsymbol{x}},\bar{\boldsymbol{u}}} \tag{39b}$$

$$\boldsymbol{C} = \frac{\partial \boldsymbol{g}(\boldsymbol{x},\boldsymbol{u})}{\partial \boldsymbol{x}}\bigg|_{\bar{\boldsymbol{x}},\bar{\boldsymbol{u}}} = \begin{bmatrix} \frac{\partial g_1(\bar{\boldsymbol{x}},\bar{\boldsymbol{u}})}{\partial x_1} & \cdots & \frac{\partial g_1(\bar{\boldsymbol{x}},\bar{\boldsymbol{u}})}{\partial x_n} \\ \vdots & \ddots & \vdots \\ \frac{\partial g_p(\bar{\boldsymbol{x}},\bar{\boldsymbol{u}})}{\partial x_1} & \cdots & \frac{\partial g_p(\bar{\boldsymbol{x}},\bar{\boldsymbol{u}})}{\partial x_n} \end{bmatrix}_{\bar{\boldsymbol{x}},\bar{\boldsymbol{u}}} \tag{39c}$$

$$\boldsymbol{D} = \frac{\partial \boldsymbol{g}(\boldsymbol{x},\boldsymbol{u})}{\partial \boldsymbol{u}}\bigg|_{\bar{\boldsymbol{x}},\bar{\boldsymbol{u}}} = \begin{bmatrix} \frac{\partial g_1(\bar{\boldsymbol{x}},\bar{\boldsymbol{u}})}{\partial u_1} & \cdots & \frac{\partial g_1(\bar{\boldsymbol{x}},\bar{\boldsymbol{u}})}{\partial u_m} \\ \vdots & \ddots & \vdots \\ \frac{\partial g_p(\bar{\boldsymbol{x}},\bar{\boldsymbol{u}})}{\partial u_1} & \cdots & \frac{\partial g_p(\bar{\boldsymbol{x}},\bar{\boldsymbol{u}})}{\partial u_m} \end{bmatrix}_{\bar{\boldsymbol{x}},\bar{\boldsymbol{u}}} \tag{39d}$$

In practice, the partial derivatives are computed numerically using a central difference scheme. For instance, the elements of the $\boldsymbol{A}$ matrix are found as follows (Refs. 41,42):

$$A_{ij} = \frac{\partial f_i(\boldsymbol{x},\boldsymbol{u})}{\partial x_j} \approx \frac{f_i(\bar{\boldsymbol{x}}+\boldsymbol{\Delta x}_j,\boldsymbol{u}) - f_i(\bar{\boldsymbol{x}}-\boldsymbol{\Delta x}_j,\boldsymbol{u})}{2\Delta x_j} \tag{40}$$

where the perturbations are performed one by one for each state. A similar procedure is adopted for finding the elements of the $\boldsymbol{B}$, $\boldsymbol{C}$, and $\boldsymbol{D}$ coefficient matrices.

Analytical Linearization Linearization via finite differences is an $O(n^2)$ time-complexity method, where n denotes the number of system states, as it requires perturbing each governing equation with respect to every state variable. To reduce the computational cost associated with this approach, an analytical differentiation of the aerodynamic system is pursued. The resulting system matrix from the analytical linearization takes the following form (Refs. 21,23):

$$\begin{Bmatrix} \Delta\dot{\boldsymbol{\mu}}_\mathrm{w} \\ \Delta\dot{\boldsymbol{\alpha}}_\mathrm{p} \\ \Delta\dot{\boldsymbol{r}}_\mathrm{p} \\ \Delta\dot{\boldsymbol{r}}_\mathrm{w} \\ \Delta\dot{\boldsymbol{\mu}}_\mathrm{b} \\ \Delta\dot{\boldsymbol{\delta}}_\mathrm{p} \end{Bmatrix} = \begin{bmatrix} \boldsymbol{A}^{\mu_\mathrm{w}}_{\mu_\mathrm{w}} & \cdots & \cdots & \boldsymbol{A}^{\mu_\mathrm{w}}_{\delta_\mathrm{p}} \\ \vdots & \ddots & & \vdots \\ \vdots & & \ddots & \vdots \\ \boldsymbol{A}^{\delta_\mathrm{p}}_{\mu_\mathrm{w}} & \cdots & \cdots & \boldsymbol{A}^{\delta_\mathrm{p}}_{\delta_\mathrm{p}} \end{bmatrix} \begin{Bmatrix} \Delta\boldsymbol{\mu}_\mathrm{w} \\ \Delta\boldsymbol{\alpha}_\mathrm{p} \\ \Delta\boldsymbol{r}_\mathrm{p} \\ \Delta\boldsymbol{r}_\mathrm{w} \\ \Delta\boldsymbol{\mu}_\mathrm{b} \\ \Delta\boldsymbol{\delta}_\mathrm{p} \end{Bmatrix} \tag{41}$$

To demonstrate the analytical linearization process, consider the time rate of change of the doublet intensities of the blade panels. Then:

$$\dot{\boldsymbol{\mu}}_\mathrm{b} = \frac{1}{\tau}\Big[-\boldsymbol{K}_9\boldsymbol{K}_3(\boldsymbol{r}_\mathrm{w})\boldsymbol{\mu}_\mathrm{w} - \boldsymbol{K}_9\boldsymbol{B}'\boldsymbol{K}_4(\boldsymbol{r}_\mathrm{p})\boldsymbol{\alpha}_\mathrm{p} + \boldsymbol{K}_9\boldsymbol{B}'(\boldsymbol{u}_\mathrm{b} - \boldsymbol{U}_\infty) - \boldsymbol{\mu}_\mathrm{b}\Big] \tag{42}$$

The perturbation form of this equation can be obtained by expanding it into a Taylor series truncated at the first order and by performing simple algebraic manipulations:

$$\begin{aligned} \Delta\dot{\boldsymbol{\mu}}_\mathrm{b} \approx & \frac{1}{\tau}\Big[-\boldsymbol{K}_9\boldsymbol{K}_3\Delta\boldsymbol{\mu}_\mathrm{w} - \boldsymbol{K}_9\boldsymbol{B}'\boldsymbol{K}_4\Delta\boldsymbol{\alpha}_\mathrm{p} - \\ & \boldsymbol{K}_9\frac{\partial \boldsymbol{K}_3}{\partial \boldsymbol{r}_\mathrm{w}}\bar{\boldsymbol{\mu}}_\mathrm{w}\Delta\boldsymbol{r}_\mathrm{w} - \boldsymbol{K}_9\boldsymbol{B}'\frac{\partial \boldsymbol{K}_4}{\partial \boldsymbol{r}_\mathrm{p}}\bar{\boldsymbol{\alpha}}_\mathrm{p}\Delta\boldsymbol{r}_\mathrm{p} + \\ & \boldsymbol{I}\,\Delta\boldsymbol{\mu}_\mathrm{b} - \boldsymbol{K}_9\boldsymbol{B}'\frac{\partial \boldsymbol{K}_4}{\partial \boldsymbol{\delta}_\mathrm{p}}\bar{\boldsymbol{\alpha}}_\mathrm{p}\Delta\boldsymbol{\delta}_\mathrm{p}\Big] \\ \approx & \boldsymbol{A}^{\mu_\mathrm{b}}_{\mu_\mathrm{w}}\Delta\boldsymbol{\mu}_\mathrm{w} + \boldsymbol{A}^{\mu_\mathrm{b}}_{\alpha_\mathrm{p}}\Delta\boldsymbol{\alpha}_\mathrm{p} + \boldsymbol{A}^{\mu_\mathrm{b}}_{r_\mathrm{w}}\Delta\boldsymbol{r}_\mathrm{w} + \boldsymbol{A}^{\mu_\mathrm{b}}_{r_\mathrm{p}}\Delta\boldsymbol{r}_\mathrm{p} + \\ & \boldsymbol{A}^{\mu_\mathrm{b}}_{\mu_\mathrm{b}}\Delta\boldsymbol{\mu}_\mathrm{b} + \boldsymbol{A}^{\mu_\mathrm{b}}_{\delta_\mathrm{p}}\Delta\boldsymbol{\delta}_\mathrm{p} \end{aligned} \tag{43}$$

The inclusion of the ground effect into the analytical linearization is in the induced velocity equations. For instance:

$$\dot{\boldsymbol{r}}^\mathrm{tot} = \dot{\boldsymbol{r}} + \dot{\boldsymbol{r}}^\mathrm{image} \tag{44}$$

It is important to note that $\dot{\boldsymbol{r}}$ is a function that depends on the inducing states and the evaluation point, and its output represents the induced velocities at that point. Accordingly, Eq. (36a) can be rewritten as:

$$\dot{\boldsymbol{r}}^\mathrm{tot}(\boldsymbol{x}^\mathrm{target},\boldsymbol{x}^\mathrm{main},\boldsymbol{x}^\mathrm{image}) = \dot{\boldsymbol{r}}(\boldsymbol{x}^\mathrm{target},\boldsymbol{x}^\mathrm{main}) + \dot{\boldsymbol{r}}(\boldsymbol{x}^\mathrm{target},\boldsymbol{x}^\mathrm{image}) \tag{45}$$

where $\boldsymbol{x}^\mathrm{target}$ are the evaluation points, which in the current case are equal to $\boldsymbol{x}^\mathrm{main}$. Now, using Taylor series expansion to get the derivatives with respect to $\boldsymbol{x}^\mathrm{main}$:

$$\frac{\partial \dot{\boldsymbol{r}}^\mathrm{tot}}{\partial \boldsymbol{x}^\mathrm{main}} = \frac{\partial \dot{\boldsymbol{r}}}{\partial \boldsymbol{x}}\bigg|_{\boldsymbol{x}^\mathrm{main}} + \frac{\partial \dot{\boldsymbol{r}}}{\partial \boldsymbol{x}}\bigg|_{\boldsymbol{x}^\mathrm{image}}\frac{\partial \boldsymbol{x}^\mathrm{image}}{\partial \boldsymbol{x}^\mathrm{main}} \tag{46}$$

where $\partial\boldsymbol{x}^\mathrm{image}/\partial\boldsymbol{x}^\mathrm{main}$ can be computed from Eq. (35).

Harmonic Decomposition

For notational simplicity, the Δ symbol is omitted, and all state and control vectors are understood as perturbations from a periodic equilibrium. The state, input, and output vectors of the Linear Time-Periodic (LTP) system are subsequently expressed using a truncated Fourier series that captures a finite number of harmonics of the fundamental period:

$$\boldsymbol{x} = \boldsymbol{x}_0 + \sum_{i=1}^{N}\left[\boldsymbol{x}_{ic}\cos\left(\frac{2\pi it}{T_\mathrm{p}}\right) + \boldsymbol{x}_{is}\sin\left(\frac{2\pi it}{T_\mathrm{p}}\right)\right] \tag{47a}$$

$$\boldsymbol{u} = \boldsymbol{u}_0 + \sum_{j=1}^{M}\left[\boldsymbol{u}_{jc}\cos\left(\frac{2\pi jt}{T_\mathrm{p}}\right) + \boldsymbol{u}_{js}\sin\left(\frac{2\pi jt}{T_\mathrm{p}}\right)\right] \tag{47b}$$

$$\boldsymbol{y} = \boldsymbol{y}_0 + \sum_{k=1}^{L}\left[\boldsymbol{y}_{kc}\cos\left(\frac{2\pi kt}{T_\mathrm{p}}\right) + \boldsymbol{y}_{ks}\sin\left(\frac{2\pi kt}{T_\mathrm{p}}\right)\right] \tag{47c}$$

The harmonic decomposition method, as detailed in Ref. 43, facilitates the transformation of the LTP system into an approximate, higher-dimensional Linear Time-Invariant (LTI) system expressed in first-order form:

$$\dot{\boldsymbol{X}} = \boldsymbol{A}\boldsymbol{X} + \boldsymbol{B}\boldsymbol{U} \tag{48a}$$
$$\boldsymbol{Y} = \boldsymbol{C}\boldsymbol{X} + \boldsymbol{D}\boldsymbol{U} \tag{48b}$$

where the augmented state vector $\boldsymbol{X} \in \mathbb{R}^{n(2N+1)}$, the augmented control vector $\boldsymbol{U} \in \mathbb{R}^{m(2M+1)}$, and the augmented output vector $\boldsymbol{Y} \in \mathbb{R}^{l(2L+1)}$ are defined as follows:

$$\boldsymbol{X}^T = \left[\boldsymbol{x}_0^T \ \boldsymbol{x}_{1c}^T \ \boldsymbol{x}_{1s}^T \ \dots \ \boldsymbol{x}_{Nc}^T \ \boldsymbol{x}_{Ns}^T\right] \tag{49a}$$
$$\boldsymbol{U}^T = \left[\boldsymbol{u}_0^T \ \boldsymbol{u}_{1c}^T \ \boldsymbol{u}_{1s}^T \ \dots \ \boldsymbol{u}_{Mc}^T \ \boldsymbol{u}_{Ms}^T\right] \tag{49b}$$
$$\boldsymbol{Y}^T = \left[\boldsymbol{y}_0^T \ \boldsymbol{y}_{1c}^T \ \boldsymbol{y}_{1s}^T \ \dots \ \boldsymbol{y}_{Lc}^T \ \boldsymbol{y}_{Ls}^T\right] \tag{49c}$$

Closed-form expressions for these matrices are detailed in Ref. 43.

Model Order Reduction

Model order reduction is performed to runtime of the linearized dynamics. Model order reduction is performed using residualization, a portion of singular perturbation pertaining to the LTI systems (Ref. 44). By assuming some fast and stable states to reach steady-state quicker than some other slow, and possibly unstable states, the state vector in Eq. (49a) can be partitioned into fast and slow components:

$$\boldsymbol{X}^T = \left[\boldsymbol{X}_{\mathrm{s}}^T \ \boldsymbol{X}_{\mathrm{f}}^T\right] \tag{50}$$

Consequently, Eqs. (48a) and (48b) can be reformulated as:

$$\begin{bmatrix}\dot{\boldsymbol{X}}_{\mathrm{s}} \\ \dot{\boldsymbol{X}}_{\mathrm{f}}\end{bmatrix} = \begin{bmatrix}\boldsymbol{A}_{\mathrm{s}} & \boldsymbol{A}_{\mathrm{sf}} \\ \boldsymbol{A}_{\mathrm{fs}} & \boldsymbol{A}_{\mathrm{f}}\end{bmatrix}\begin{bmatrix}\boldsymbol{X}_{\mathrm{s}} \\ \boldsymbol{X}_{\mathrm{f}}\end{bmatrix} + \begin{bmatrix}\boldsymbol{B}_{\mathrm{s}} \\ \boldsymbol{B}_{\mathrm{f}}\end{bmatrix}\boldsymbol{U} \tag{51a}$$
$$\boldsymbol{Y} = \begin{bmatrix}\boldsymbol{C}_{\mathrm{s}} & \boldsymbol{C}_{\mathrm{f}}\end{bmatrix}\begin{bmatrix}\boldsymbol{X}_{\mathrm{s}} \\ \boldsymbol{X}_{\mathrm{f}}\end{bmatrix} + \boldsymbol{D}\boldsymbol{U} \tag{51b}$$

By neglecting the dynamics of the fast states, effectively setting $\dot{\boldsymbol{X}}_{\mathrm{f}} = 0$, a reduced-order system with a state vector comprising only the slow states can be derived. This is achieved by solving the $\dot{\boldsymbol{X}}_{\mathrm{f}}$ equation for $\boldsymbol{X}_{\mathrm{f}}$ and substituting the resulting expression into the $\dot{\boldsymbol{X}}_{\mathrm{s}}$ and $\boldsymbol{Y}_{\mathrm{s}}$ equations:

$$\dot{\boldsymbol{X}}_{\mathrm{s}} = \hat{\boldsymbol{A}}\boldsymbol{X}_{\mathrm{s}} + \hat{\boldsymbol{B}}\boldsymbol{U} \tag{52a}$$
$$\boldsymbol{Y}_{\mathrm{s}} = \hat{\boldsymbol{C}}\boldsymbol{X}_{\mathrm{s}} + \hat{\boldsymbol{D}}\boldsymbol{U} \tag{52b}$$

where:

$$\hat{\boldsymbol{A}} = \boldsymbol{A}_{\mathrm{s}} - \boldsymbol{A}_{\mathrm{sf}}\boldsymbol{A}_{\mathrm{f}}^{-1}\boldsymbol{A}_{\mathrm{fs}} \tag{53a}$$
$$\hat{\boldsymbol{B}} = \boldsymbol{B}_{\mathrm{s}} - \boldsymbol{A}_{\mathrm{sf}}\boldsymbol{A}_{\mathrm{f}}^{-1}\boldsymbol{B}_{\mathrm{f}} \tag{53b}$$
$$\hat{\boldsymbol{C}} = \boldsymbol{C}_{\mathrm{s}} - \boldsymbol{C}_{\mathrm{f}}\boldsymbol{A}_{\mathrm{f}}^{-1}\boldsymbol{A}_{\mathrm{fs}} \tag{53c}$$
$$\hat{\boldsymbol{D}} = \boldsymbol{D} - \boldsymbol{C}_{\mathrm{f}}\boldsymbol{A}_{\mathrm{f}}^{-1}\boldsymbol{B}_{\mathrm{f}} \tag{53d}$$

In this analysis, the zeroth harmonic states are selected as the slow states, while the higher harmonic states are designated as the fast states.

RESULTS

The SSPVVPM method was integrated with a rotor simulation model with properties similar to the UH-60 rotor (Table 1). The simulation model is developed in MATLAB®.

Table 1: Geometric characteristics and rotational speed of the UH-60-like main rotor blade (Ref. 45).

Parameter	Value	Units
Radius, R	8.168	m
Blade chord, c	0.527	m
Blade twist, θ_{tw}	-13	deg
Flapping hinge offset, r_{c}	0.381	m
Angular speed, Ω	27	rad/s

Nonlinear Dynamics

A four-bladed rotor configuration is used to validate the nonlinear dynamics, incorporating a total of 43,696 states. The discretization includes 5×10 near-wake panels, 10×10 surface panels per blade, and 150×10 vortex particles distributed along the chord and span. The nonlinear dynamics are validated against experimental and computational work.

Figure 3 shows the computed thrust ratio, $T_{\mathrm{IGE}}/T_{\mathrm{OGE}}$, as a function of the non-dimensional height above ground, $\mathrm{z/R}$. The numerical predictions are compared against experimental data from Leishman (OH-6A, OH-58A, UH-1H, and UH-1C) (Ref. 46) , Light (Ref. 36), Borisov et al. (Ref. 47), Fradenburgh (Ref. 48), and Cheeseman et al. (Ref. 49) and as well as computational results from Zhao et al. (Ref. 50). The current simulation results lie within the range of both experimental and numerical results, demonstrating the solver's ability to capture the essential aerodynamic characteristics of ground effect. Notably, the results reflect the nonlinear increase in thrust as the rotor descends below $\mathrm{z/R} = 1$, consistent with experimental expectations. Note that the current solver was validated against experimental work for the OGE condition in Refs. 23, 25.

The radial distribution of thrust coefficient is shown in Fig. 4 for different ground proximities. From Fig. 4, it can be seen that as the rotor descends closer to the ground, the peak of the circulation distribution shifts inboard, and the overall unsteadiness increases. At higher altitudes ($\mathrm{z/R} \geq 4$), the radial load distribution stays

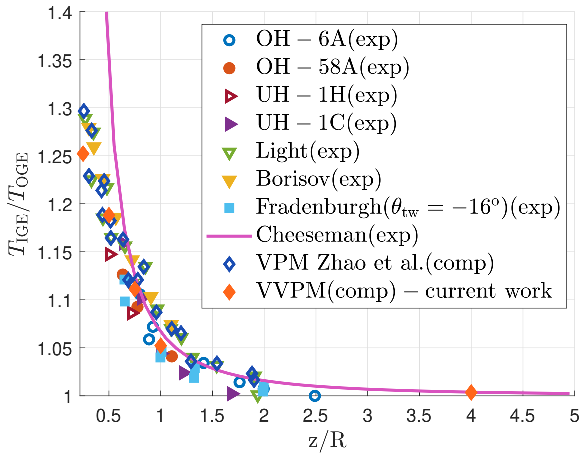

Figure 3: $T_{\mathrm{IGE}}/T_{\mathrm{OGE}}$ comparison.

mostly similar to the OGE condition. However, as the rotor approaches the ground, the influence of returning tip vortices causes the radial load to spread more evenly along the span. This contrasts with the OGE case, where the returning tip vortices primarily affect the blade near its tip.

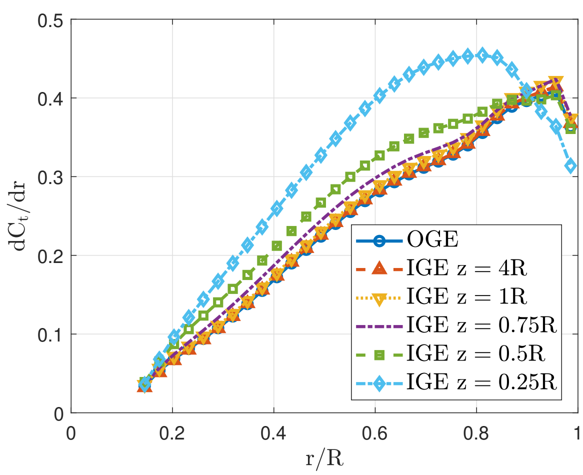

Figure 4: Radial load Comparison at different z/R.

Figure 5 visualizes the wake structure for various ground heights. For OGE and IGE at $z/R = 4$, there is no significant change in the wake structure, which is also evident in Figs. 3 and 4. As the rotor gets closer to the ground, the wake starts to compress about the ground location, increasing the thrust of the rotor. Notably, the lateral contraction in the wake fades out as the rotor gets closer to the ground plane ($z/R < 1.0$), as evident in Ref. 26. Additionally, because of the ground effect, vortex particles near the rotor hub, which are typically weaker due to low bound circulation and smaller inflow, tend to get deflected upward. Since they have less inertia and are more easily influenced by local velocity fields, they lift up instead of remaining in the wake plane. This creates a pronounced upward deflection in the inner cutout region of the rotor disc, forming a fountain-like structure. A similar pattern can be observed in the wake visualizations presented in Ref. 51. Also, it is worth noting that when the ground plane is placed very close to the rotor, some particles may pass below the ground level. This nonphysical phenomenon occurs because the method of images models the ground effect without enforcing a physical boundary. The issue becomes more noticeable under extreme IGE conditions and can be influenced by large time steps or steep inflow gradients.

As discussed in Refs. 25, 26, the inclusion of viscous effects improves the fidelity of wake modeling near the ground. In this work, the influence of viscosity is examined by comparing both the wake structure and resulting loads for viscous and inviscid formulations. Viscosity is incorporated through the diffusion term $\nu_\infty \nabla^2 \boldsymbol{\omega}$ in the vorticity transport equation (Eq. (2)), and numerically implemented using the Particle Strength Exchange (PSE) scheme (Ref. 32).

Figure 6 illustrates the rotor wake structure in OGE and IGE conditions at two representative heights ($z/R = 1$ and $z/R = 0.5$) for both the viscous and inviscid cases. In the OGE case, the influence of viscosity on the wake structure becomes noticeable. When viscous effects are included, the wake exhibits reduced contraction compared to the inviscid case. This is primarily due to the diffusion of vorticity, which weakens the strength of the wake and leads to a more spread-out flow field. As a result, the overall wake contraction is less pronounced when viscosity is taken into account (Ref. 46). In the IGE cases, the influence of viscosity is apparent as well. Without viscosity, the wake remains highly organized and compact. When viscosity is included, the wake shows increased diffusion and broader vorticity spreading, reducing the coherence of the wake structure.

To further examine the influence of viscosity on ground effect predictions, the normalized thrust ratio $T_{\mathrm{IGE}}/T_{\mathrm{OGE}}$ is plotted in Fig. 7 for both the VPM and VVPM solvers. As shown, the inviscid VPM tends to overpredict thrust in ground effect, primarily because the vorticity in the rotor wake and its image system remains undiffused, leading to stronger induced velocities and, consequently, greater thrust augmentation. Notably, the difference between the viscous and inviscid cases diminishes at very low altitudes ($z/R \leq 0.5$). This can be attributed to the limited spatial and temporal extent available for viscous effects to develop. At such close proximities to the ground, the increase in thrust is governed predominantly by near-field pressure accumulation rather than wake-induced flow modifications, making the influence of viscosity less pronounced.

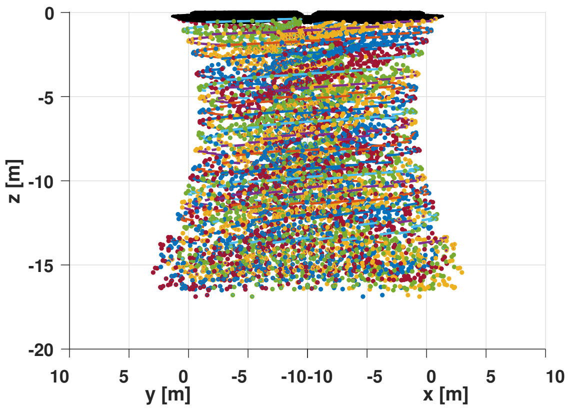

(a) OGE.

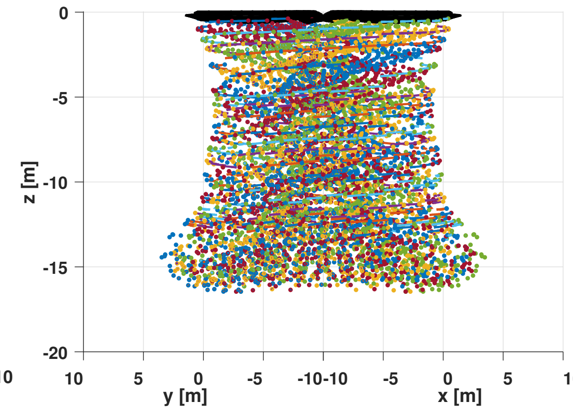

(b) IGE z/R = 4, GP @ z = -32.67 m

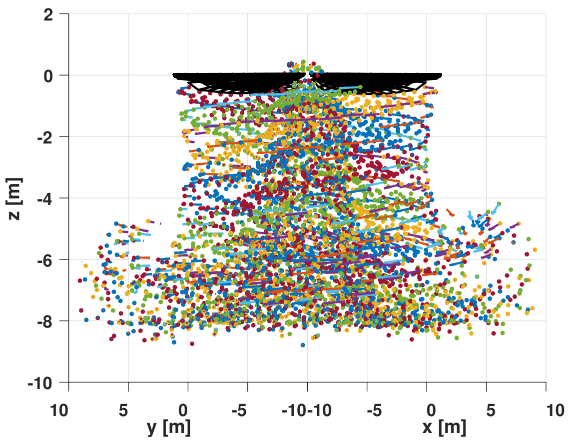

(c) IGE z/R = 1, GP @ z = -8.17 m

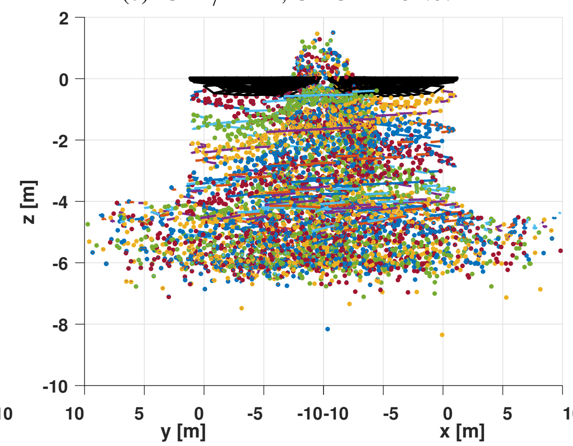

(d) IGE z/R = 0.75, GP @ z = -6.13 m

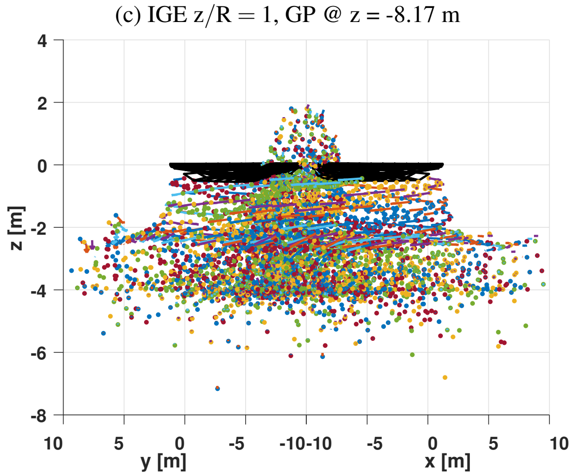

(e) IGE z/R = 0.5, GP @ z = -4.08 m

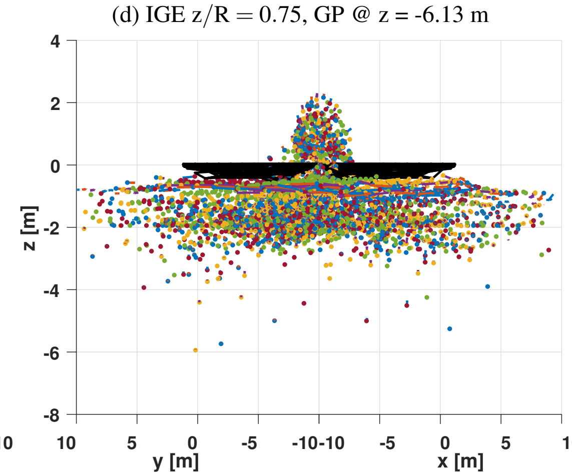

(f) IGE z/R = 0.25, GP @ z = -2.04 m

Figure 5: Wake structure variation with z/R.

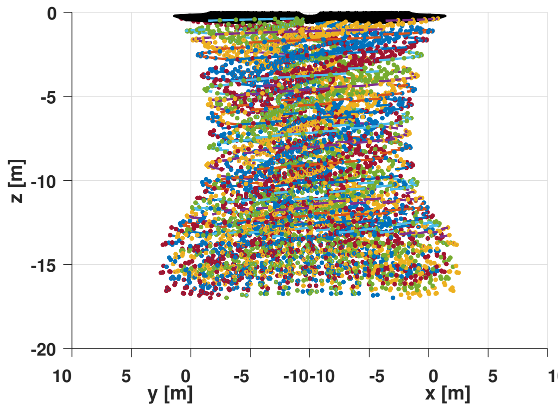

(a) OGE without viscosity.

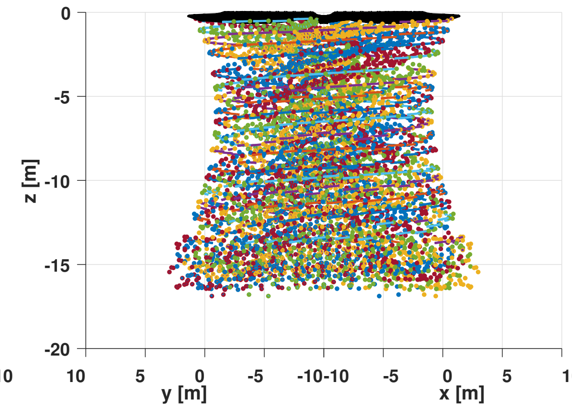

(b) OGE with viscosity.

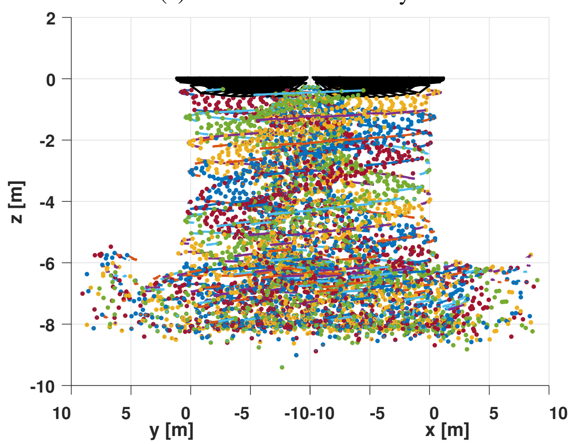

(c) IGE $z/R = 1$ without viscosity.

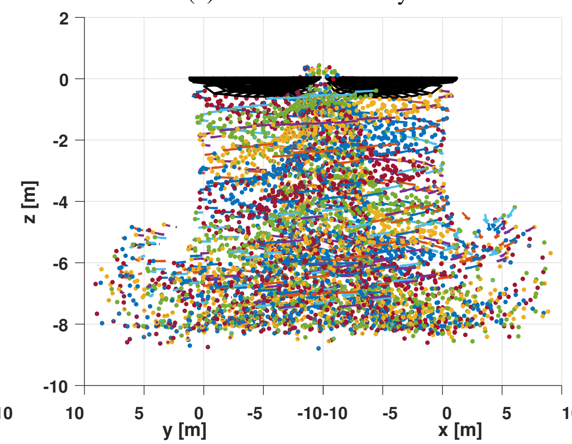

(d) IGE $z/R = 1$ with viscosity.

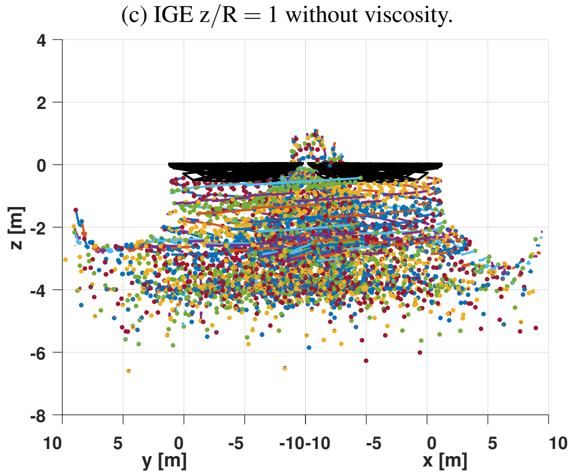

(e) IGE $z/R = 0.5$ without viscosity.

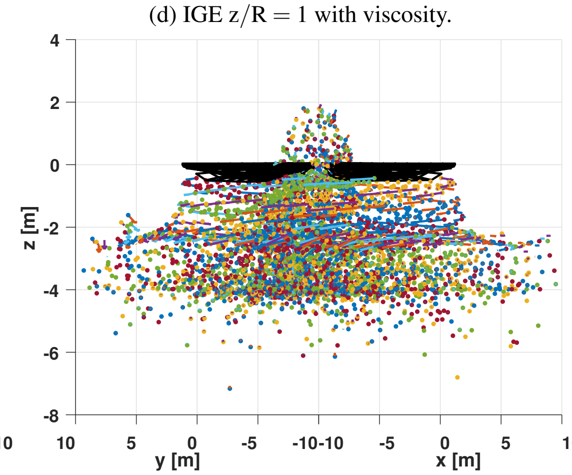

(f) IGE $z/R = 0.5$ with viscosity.

Figure 6: Wake structure with z/R with and without viscosity.

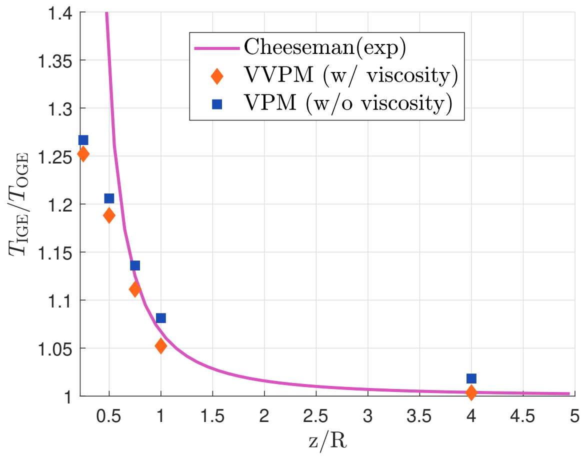

Figure 7: $T_{\text{IGE}}/T_{\text{OGE}}$ with and without viscosity comparison.

Linear Dynamics

The nonlinear dynamics were linearized about the periodic equilibrium over one rotor revolution, forming an LTP system. Harmonic decomposition was then applied to approximate this system as a high-order LTI model, retaining the first state and output harmonics ($N = L = 1$ in Eqs. (47a)–(47c)) and only the zeroth harmonic of the control input ($M = 0$), consistent with low-frequency control inputs such as primary flight controls. The truncation of harmonics constitutes an implicit model reduction, with the final LTI model comprising 22,272 states, 3 control inputs, and 309 outputs.

Figure 8a compares eigenvalues from the high-order LTI model obtained via analytical and numerical linearization for IGE $\text{z}/\text{R} = 1$, showing acceptable agreement. Furthermore, Figure 8b shows the eigenvalue distribution of both the full and reduced-order systems, exhibiting a characteristic "cloud" structure typical of rotary-wing systems with tip-vortex dynamics (Refs. 12, 52).

The computational time advantages of analytical linearization were evaluated by comparing the processing times of numerical and analytical methods across a range of state dimensions. As illustrated in Figure 16, the analytical approach demonstrates a reduction in computational complexity of $\text{O}(n^2)$, where n represents the number of states. Additionally, it can be seen that the inclusion of the ground effect has a higher contribution to the numerical linearization cost than the analytical linearization cost.

Time-Domain Verification

The linearized models were validated in the time domain by comparing their responses to a 2° collective pitch doublet input against the nonlinear system response. The

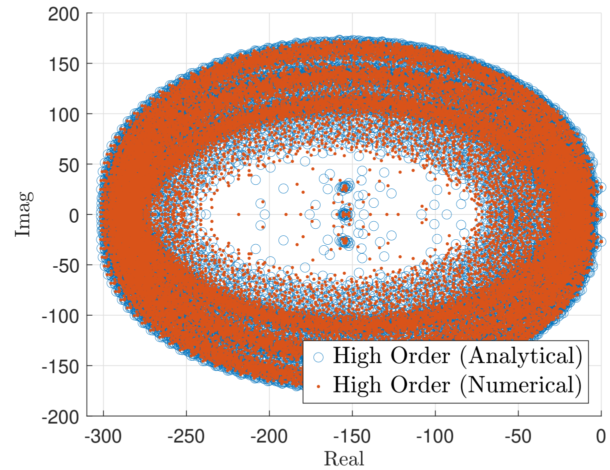

(a) High order analytical linear and high order numerical linear systems.

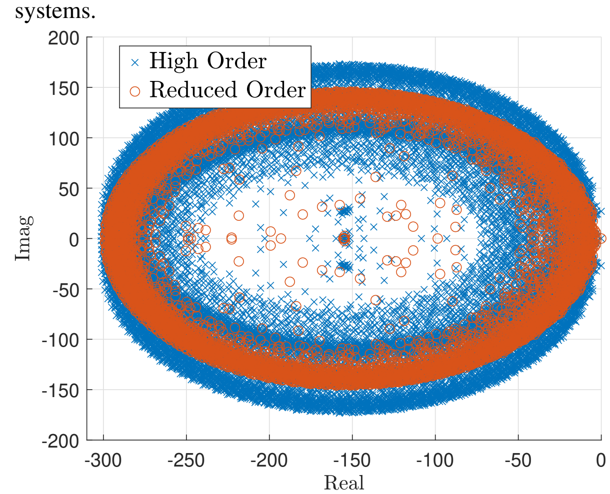

(b) High order analytical linear and reduced-order analytical linear systems.

Figure 8: Eigenvalues of the coupled panel and viscous vortex particle linear dynamics for IGE $\text{z}/\text{R} = 1$.

nonlinear time histories were obtained by integrating Eqs. (13), while the harmonic decomposition model was integrated via Eq. (48), and the residualized dynamics via Eqs. (52a) and (52b).

To evaluate discrepancies in the wake dynamics, selected states and the vertical load were examined. Figure 10 compares the nonlinear, numerically linearized, and analytically linearized responses for these quantities for IGE $\text{z}/\text{R} = 1$. Figure 11 further compares the nonlinear response with both the high-order and reduced-order analytical models. Linearized output perturbations were reconstructed using Eq. (47c), while state perturbations from the high-order model were reconstructed using Eq. (47a).

A minor discrepancy in $\boldsymbol{\delta}_\text{p}$ is observed in Figs. 10 and 11, attributed to the nonlinear evolution of particle core radii in Eq. (28f), which is not fully captured by the linear

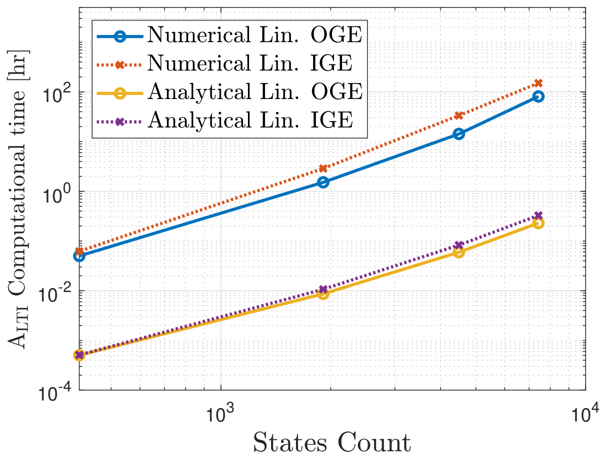

Figure 9: Linearization cost vs. states count of the coupled panel and viscous vortex particle dynamics IGE and OGE.

models. Nevertheless, Fig. 11 shows excellent agreement between the nonlinear, high-order, and reduced-order analytical models. These results confirm the accuracy and robustness of the linearization approach.

The comparison between the OGE and the IGE cases is extended to include the linearized system dynamics. Figure 12a shows the vertical load response for OGE, IGE at $z/R = 1$, and IGE at $z/R = 0.5$, resulting from a doublet collective input. As seen in Fig. 12a, the linearized model successfully captures the dominant aerodynamic behavior. Additionally, Fig. 12b presents the corresponding mean inflow λ_0 responses for the same conditions and input. The observed discrepancies between the linear and nonlinear solvers in predicting the mean inflow response can be attributed to nonlinear dependencies in the inflow calculation, particularly $\boldsymbol{\alpha}_{\mathrm{p}}$, $\boldsymbol{r}_{\mathrm{p}}$, and $\boldsymbol{\delta}_{\mathrm{p}}$, which are not fully captured by the linearized dynamics. Overall, the analytical and numerical linearization schemes show excellent agreement, demonstrating the potential of the analytical approach to serve as an effective replacement for numerical linearization. Furthermore, from Figs. 12a and 12b, it can be seen that as the rotor gets closer to the ground, the thrust increases and the mean inflow decreases, consistent with the observations in Refs. 53, 54.

Frequency-Domain Verification

To further validate the linearized models, their frequency responses are compared against those extracted from the nonlinear system using standard frequency sweep techniques (Ref. 55). The nonlinear model is excited with a range of frequencies in the collective pitch input, and the resulting responses in the selected states and vertical load are recorded. These input-output datasets are then used to compute the corresponding frequency responses. For the linearized models, frequency responses are obtained directly from their state-space representations. A Fast Fourier Transform (FFT) is applied using a 20-second Hamming window with a 0.8 overlap fraction. This comparison enables the assessment of how accurately the linearized models capture the system's behavior across a range of frequencies.

Figure 13 compares the frequency responses of selected states and outputs from the nonlinear model, the high-order analytical linearization, and the high-order numerical linearization for IGE $z/R = 1$. Overall, the linearized models show good agreement with the nonlinear system at low frequencies, particularly in terms of magnitude and phase response.

For $\boldsymbol{\mu}_{\mathrm{w}}$, $\boldsymbol{\alpha}_{\mathrm{p}}$, and $\boldsymbol{\mu}_{\mathrm{b}}$ (Figs. 13a, 13b, and 13e), the linearized models closely match the nonlinear behavior across most frequencies, with coherence remaining acceptable. Deviations at higher frequencies are minimal. In contrast, $\boldsymbol{r}_{\mathrm{w}}$ and $\boldsymbol{r}_{\mathrm{p}}$ (Figs. 13c and 13d) exhibit larger discrepancies at mid-to-high frequencies, particularly in magnitude, indicating nonlinear interactions not captured by the linear models. For $\boldsymbol{\delta}_{\mathrm{p}}$ (Fig. 13f), notable discrepancies appear around 1 rad/s, accompanied by a significant drop in coherence. However, the responses realign at higher frequencies, likely due to the reduced influence of nonlinear core-radius evolution.

It is worth noting that deviations around 1 rad/s may be partially attributed to spectral leakage and windowing artifacts from the FFT process, rather than purely physical dynamics. The coherence trends support this interpretation, as reduced coherence in this region suggests noise and numerical limitations in the frequency-domain estimation. Overall, the results confirm that the linearized models provide accurate predictions of the system's low-frequency behavior, with increasing deviation as nonlinear and unmodeled dynamics become more significant at higher frequencies.

Figure 14 shows the frequency response comparison for selected states across the nonlinear model, high-order analytical linear model, and reduced-order analytical linear model. At low frequencies, the reduced-order model generally follows both the nonlinear and high-order models closely in terms of both magnitude and phase. This is particularly clear for $\boldsymbol{\mu}_{\mathrm{w}}$ (Fig. 14a), $\boldsymbol{\alpha}_{\mathrm{p}}$ (Fig. 14b), $\boldsymbol{r}_{\mathrm{w}}$ (Fig. 14c), and $\boldsymbol{\mu}_{\mathrm{b}}$ (Fig. 14e), where the response shapes match well.

As the frequency increases, some differences start to appear. For $\boldsymbol{\mu}_{\mathrm{w}}$, the reduced-order model starts to drift from the other two models, especially beyond the mid-frequency range. A similar pattern is seen for $\boldsymbol{\alpha}_{\mathrm{p}}$, where the reduced-order model no longer tracks the high-order and nonlinear responses as well. In the case of $\boldsymbol{r}_{\mathrm{w}}$, the agreement holds over the whole frequency range. For

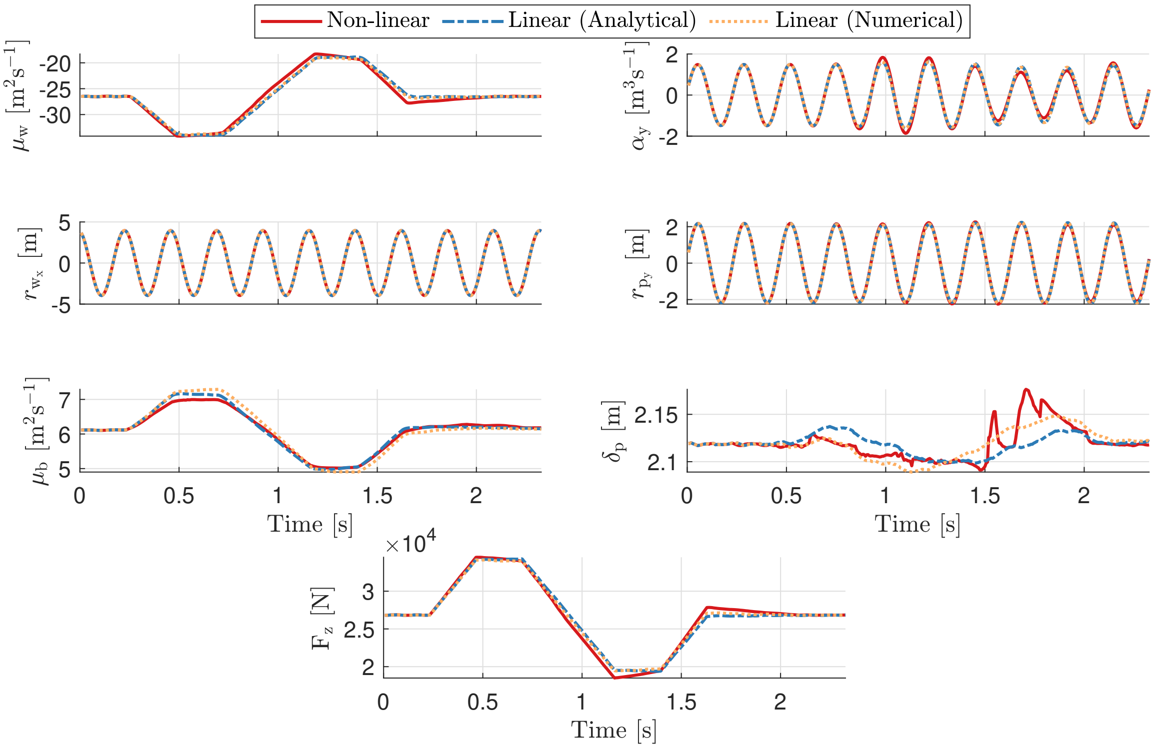

Figure 10: Nonlinear vs linear solvers for a 2 deg doublet input IGE $z/R = 1$.

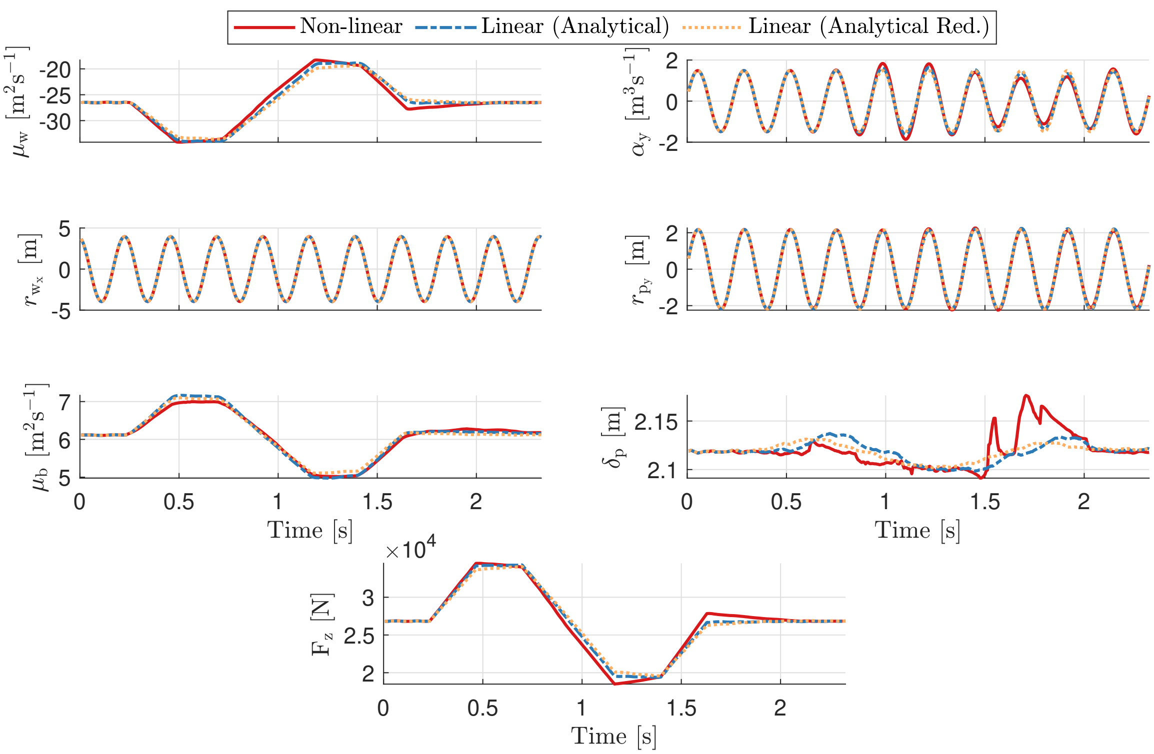

Figure 11: Nonlinear vs analytical linear solver (high-order model and reduced-order model) for a 2 deg doublet input IGE $z/R = 1$.

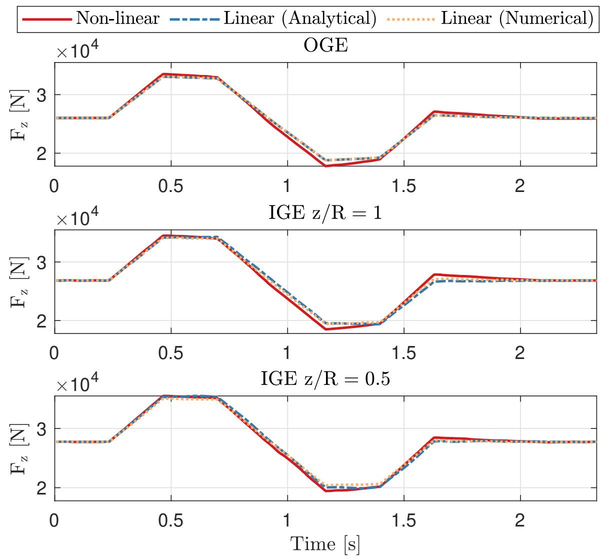

(a) Vertical Load F_z

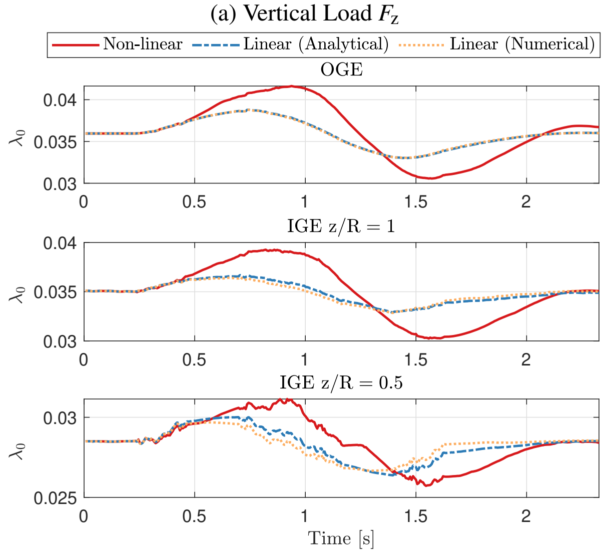

(b) Mean inflow λ_0

Figure 12: Time history as a result of 2-deg doublet collective input for OGE, IGE $z/R = 1$, and IGE $z/R = 0.5$.

$\boldsymbol{r}_p$ (Fig. 14d), the magnitude stays consistent up to high frequencies, but the phase response starts to differ noticeably at higher frequencies, likely due to nonlinear effects. The response for $\boldsymbol{\mu}_b$ stays consistent across the full range, with only small phase differences, suggesting the reduced-order model works well for that state. Finally, for $\boldsymbol{\delta}_p$ (Fig. 14f), the reduced-order model begins to break down around mid-frequencies, with mismatches in both magnitude and phase and a clear drop in coherence.

In summary, the reduced-order model provides a good match at low frequencies, but its accuracy drops off at higher frequencies where nonlinearities and unmodeled dynamics become more significant.

Figure 15 shows the frequency response of the vertical load F_z. In Fig. 15a, the nonlinear, high-order numerical, and high-order analytical models are in close agreement with a minor phase shift, consistent with the time-domain trends in Fig. 10. Figure 15b compares the nonlinear, high-order, and reduced-order analytical models. The reduced-order response shows some mismatch, particularly at higher frequencies, following the same pattern seen in Fig. 11. Still, the coherence remains high across the frequency range, suggesting that nonlinearities have limited impact on the vertical load.

It is important to emphasize that the time and frequency responses presented for selected states are meant to illustrate representative aspects of the system's behavior rather than imply consistent dynamics across all states. Differences in individual responses may arise due to variations in their dynamic characteristics. However, integral quantities such as the vertical load and mean inflow provide a more complete picture of the overall system dynamics.

Computational Cost Study

Following the validation of the linearized dynamics in time and frequency domains, the computational speedup was evaluated across varying state dimensions. Simulations were conducted on an AMD® Core™ EPYC 9754 processor with 128 physical cores, where nonlinear simulations utilized parallelization, while linearized models were executed on a single core. As illustrated in Fig. 16, the linearized models, particularly the reduced order form, offer substantial computational advantages compared to the parallelized nonlinear solver. Results indicate a potential three-order-of-magnitude speedup if the nonlinear solver were executed on a single core. However, the relative speedup decreases with increasing state count, narrowing the runtime gap between nonlinear and linearized simulations. Additional speed improvements may be achievable through the parallelization of the linearized solvers.

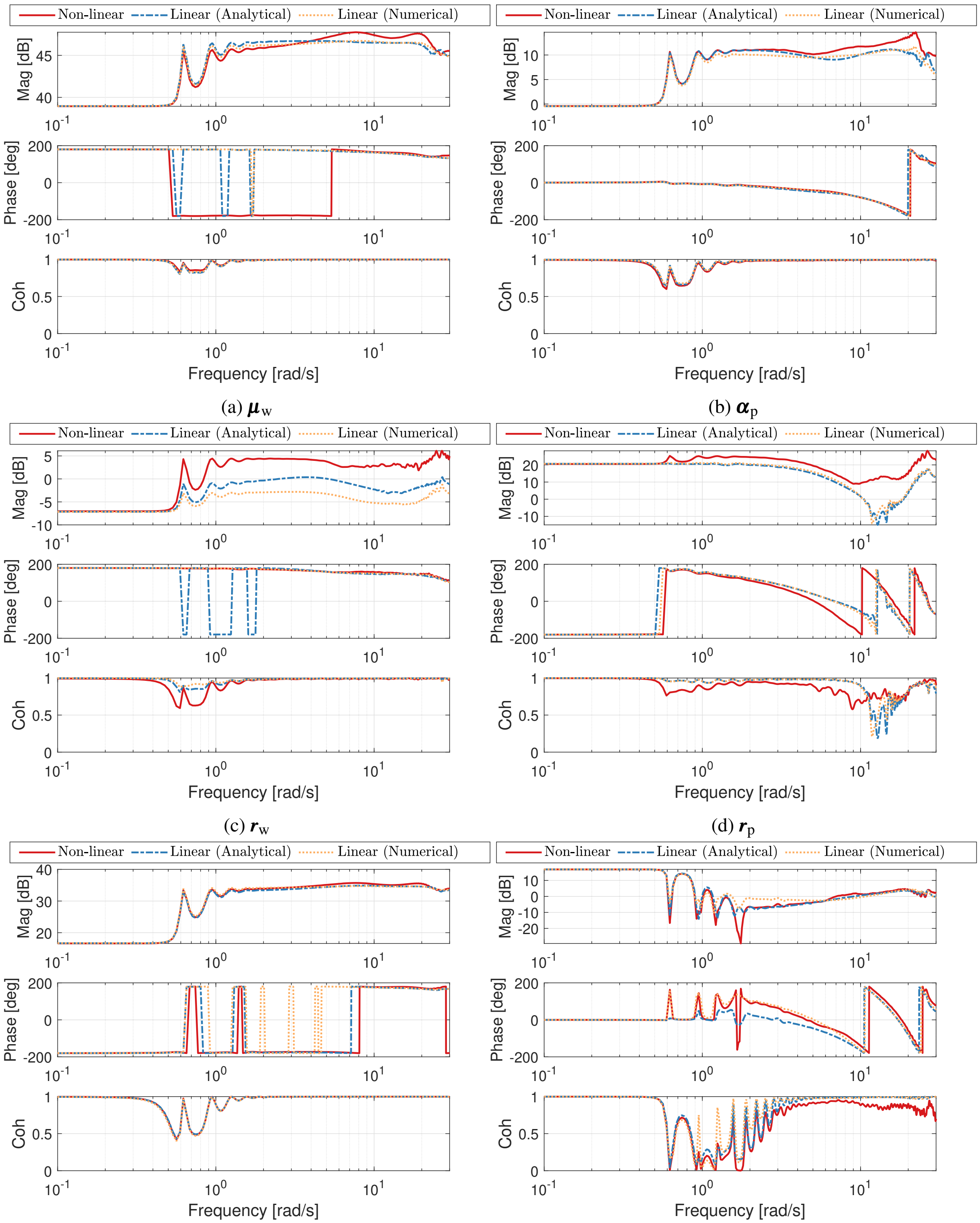

(a) $\boldsymbol{\mu}_{\mathrm{w}}$
(b) $\boldsymbol{\alpha}_{\mathrm{p}}$
(c) $\boldsymbol{r}_{\mathrm{w}}$
(d) $\boldsymbol{r}_{\mathrm{p}}$
(e) $\boldsymbol{\mu}_{\mathrm{b}}$
(f) $\boldsymbol{\delta}_{\mathrm{p}}$

Figure 13: Frequency response of the selected states: non-linear, high-order linear analytical, and high-order linear numerical IGE $z/R = 1$.

CONCLUSIONS AND FUTURE WORK

This work presents an enhanced state-space aerodynamic solver that integrates ground effect using the method of images within a coupled panel and viscous vortex particle method. The resulting formulation enables model-

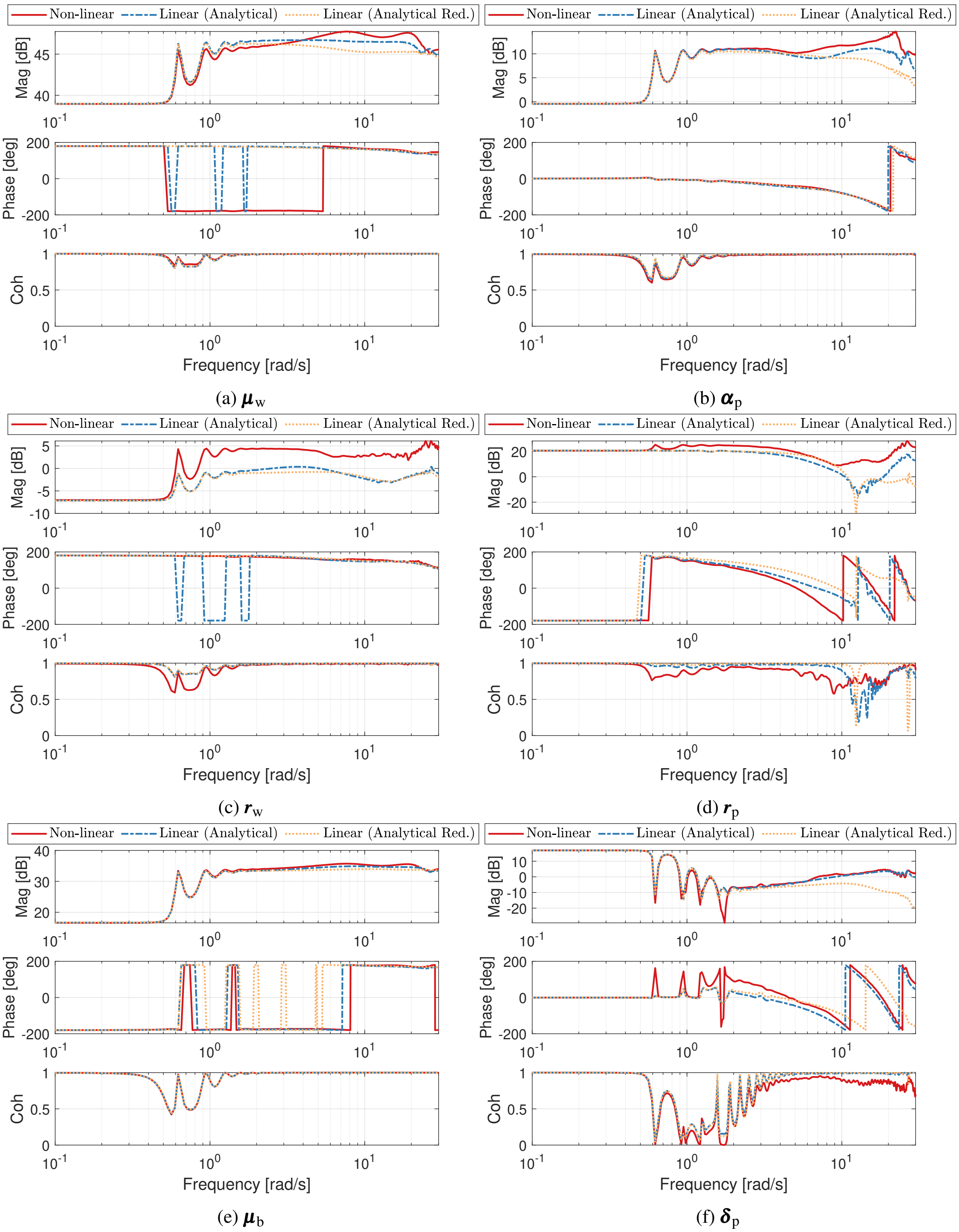

Figure 14: Frequency response of some of the selected states: non-linear, high-order linear analytical, and reduced-order linear analytical IGE $z/R = 1$.

ing of rotorcraft wake-ground interaction while preserving the state-space structure necessary for linear systems analysis. The solver supports both analytical and numerical linearization techniques, and the full nonlinear model

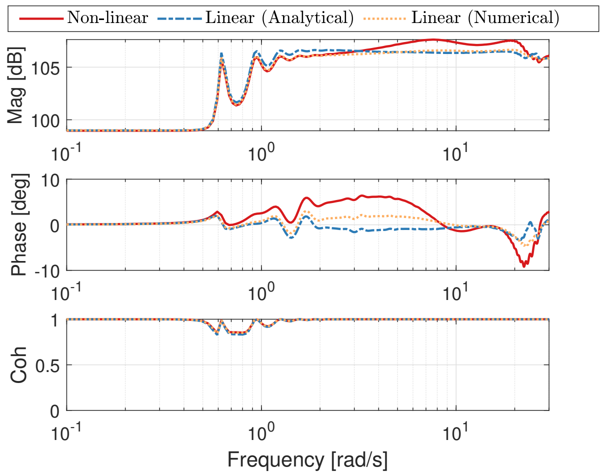

(a) Nonlinear, numerical linear, and analytical linear

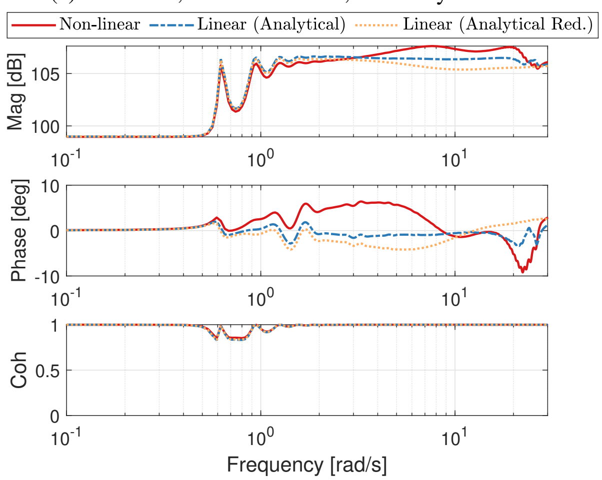

(b) Nonlinear, analytical linear (full order), and analytical linear (reduced order)

Figure 15: Frequency response of the load F_z IGE $z = 1R$.

was validated against experimental data and high-fidelity numerical simulations. The linearized models were rigorously verified against the nonlinear dynamics across varying ground proximities, demonstrating good agreement in both time and frequency domains.

Results indicate that the full linear model captures low- and mid-frequency dynamics effectively, with only minor discrepancies observed at higher frequencies. The proposed analytical linearization approach matches the accuracy of numerical perturbation methods while offering significantly reduced computational cost, scaling as $O(n^2)$. Reduced-order models also demonstrate acceptable performance, particularly in the low-to-mid frequency range, although their accuracy diminishes at higher frequencies, limiting their applicability in broadband or highly dynamic scenarios.

Future work will expand the solver's capabilities to include inclined ground surfaces (Refs. 53, 56), and to model forward flight conditions under both OGE and IGE conditions. Additionally, it will implement and linearize the other techniques mentioned previously to incorporate the ground effect.

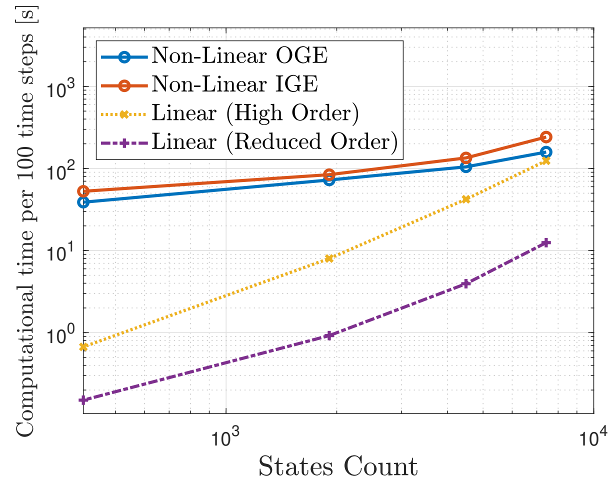

Figure 16: Simulation speed up for varying number of states OGE and IGE.

Author contact:
Hussien Hussien hhussien@umd.edu
Umberto Saetti saetti@umd.edu.

ACKNOWLEDGMENTS

This research was partially funded by the U.S. Government under agreement no. N00014-22-1-2342. The views and conclusions contained in this document are those of the authors and should not be interpreted as representing the official policies, either expressed or implied, of the Aviation Development Directorate or the U.S. Government.

REFERENCES

1. Jude, D., Lee, B., Jung, Y. S., Petermann, J., Govindarajan, B., and Bader, J., "Application of a Heterogeneous CFD Framework Towards Simulating Complete Rotorcraft Configurations," Proceedings of the 74th Annual Forum of the Vertical Flight Society (VFS), May 2018. DOI: https://doi.org/10.4050/F-0074-2018-12835

2. Peters, N., and Shirazi, D., "On the Application of an Actuator Line Model for Rotorcraft Outwash Predictions," AIAA SCITECH 2025 Forum, Jan 2025. DOI: https://doi.org/10.2514/6.2025-1753

3. Horn, J. F., Bridges, D. O., Wachspress, D. A., and Rani, S. L., "Implementation of a Free-Vortex Wake Model in Real-Time Simulation of Rotorcraft," *AIAA Journal of Computing, Information, and Communications*, Vol. 3, (3), Mar 2006, pp. 93–107. DOI: https://doi.org/10.2514/1.18273

4. Keller, J. D., Wachspress, D. A., and Hoffler, J. C., "Real Time Free Wake and Ship Airwake Model for Rotorcraft Flight Training Applications," Proceedings of the 71st Annual Forum of the American Helicopter Society, May 5-7 2015. DOI: https://doi.org/10.4050/F-0071-2015-10210

5. Theron, J. P., Horn, J. F., and Wachspress, D. A., "An integrated simulation tool for e-VTOL aeromechanics and flight control analysis," Aeromechanics for Advanced Vertical Flight Technical Meeting, San Jose, CA, Jan 21-23, 2020.

6. Zhao, J., and He, C., "A Viscous Vortex Particle Model for Rotor Wake and Interference Analysis," *Journal of the American Helicopter Society*, Vol. 55, (1), Jan 2010, pp. 1–14. DOI: https://doi.org/10.4050/JAHS.55.012007

7. He, C., "Modeling the Aerodynamic Interaction of Multiple Rotor Vehicles and Compound Rotorcraft with Viscous Vortex Particle Method," 72nd Annual Forum of the Vertical Flight Society, May 2016. DOI: https://doi.org/10.4050/F-0072-2016-11493

8. Celi, R., "State-Space Representation of Vortex Wakes by the Method of Lines," *Journal of the American Helicopter Society*, Vol. 50, (2), 2005, pp. 195–205. DOI: https://doi.org/10.4050/1.3092855

9. Bagai, A., and Leishman, G. J., "Rotor Free-Wake Modeling Using a Pseudo-Implicit Technique—Including Comparison with Experimental Data," *Journal of the American Helicopter Society*, Vol. 40, (3), Jul 1995, pp. 29–41. DOI: https://doi.org/10.4050/JAHS.40.29

10. Bhagwat, M. J., *Transient Dynamics of Helicopter Rotor Wakes Using a Time-Accurate Free-Vortex Method*, Ph.D. thesis, University of Maryland, College Park, MD, 2001. DOI: https://doi.org/10.2514/6.2001-993

11. Horn, J. F., "Non-Linear Dynamic Inversion Control Design for Rotorcraft," *Aerospace*, Vol. 6, (38), 2019. DOI: https://doi.org/10.3390/aerospace6030038

12. Saetti, U., and Horn, J. F., "Implementation and Linearization of State-Space Free-Vortex Wake Models for Rotary- and Flapping-Wing Vehicles," *Journal of the American Helicopter Society*, Vol. 68, (4), Apr 2023, pp. 42004–42017. DOI: https://doi.org/10.4050/JAHS.68.042004

13. Winckelmans, G. S., *Topics in vortex methods for the computation of three-and two-dimensional incompressible unsteady flows*, Ph.D. thesis, California Institute of Technology, 1989. DOI: https://doi.org/10.7907/19HD-DF80

14. Mimeau, C., and Mortazavi, I., "A review of vortex methods and their applications: From creation to recent advances," *Fluids*, Vol. 6, (2), 2021, pp. 68. DOI: https://doi.org/10.3390/fluids6020068

15. Savino, A., Cocco, A., Zanoni, A., Zanotti, A., and Muscarello, V., "A Coupled Multibody -Mid Fidelity Aerodynamic Tool for the Simulation of Tiltrotor Manoeuvres," Proceedings of the 47th European Rotorcraft Forum, 09 Sep 6-9, 2021.

16. He, C., and Zhao, J., "Modeling Rotor Wake Dynamics with Viscous Vortex Particle Method," *AIAA Journal*, Vol. 47, (4), 2009, pp. 902–915. DOI: https://doi.org/10.2514/1.36466

17. Lu, Y., Su, T., Chen, R., Li, P., and Wang, Y., "A method for optimizing the aerodynamic layout of a helicopter that reduces the effects of aerodynamic interaction," *Aerospace Science and Technology*, Vol. 88, 2019, pp. 73 – 83. DOI: https://doi.org/10.1016/j.ast.2019.03.005

18. Tan, J., Zhou, T., Sun, J., and Barakos, G. N., "Numerical investigation of the aerodynamic interaction between a tiltrotor and a tandem rotor during shipboard operations," *Aerospace Science and Technology*, Vol. 87, 2019, pp. 62–72. DOI: https://doi.org/10.1016/j.ast.2019.02.005

19. Alvarez, E., and Ning, A., "Development of a Vortex Particle Code for the Modeling of Wake Interaction in Distributed Propulsion," AIAA Applied Aerodynamics Conference, Atlanta, GA, Jun 2018. DOI: https://doi.org/10.2514/6.2018-3646

20. Hussien, H., Cocco, A., and Saetti, U., "Implementation, Linearization, and Order Reduction of a Coupled Panel and Free-Wake Method in State-Space Form," AIAA SciTech 2024 Forum, Jan 8–12, 2024. DOI: https://doi.org/10.2514/6.2024-2265

21. Hussien, H., Cocco, A., and Saetti, U., "Implementation and Linearization of a Coupled Panel and Vortex Particle Method in State-Space Form," *AIAA Journal*, Vol. 62, Jul 2024. DOI: https://doi.org/10.2514/1.J063855

22. Hussien, H., Cocco, A., and Saetti, U., "Implementation of a Rotor Simulation with a Coupled Panel and Vortex Particle Method in State-Space Form," 6th Decennial VFS Aeromechanics Specialists' Conference, 02 Feb 6-8, 2024.

23. Hussien, H., Cocco, A., and Saetti, U., "Implementation and Analytical Linearization of a Rotor Simulation with a Coupled Panel and Vortex Particle Method in State-Space Form," *Journal of the American Helicopter Society*, Jan 2025. DOI: https://doi.org/10.4050/JAHS.70.022003

24. Hussien, H., and Saetti, U., "Fast Multipole Method for a Rotor Simulation With a State-Space Vortex Particle Method," AIAA SCITECH 2025 Forum. DOI: https://doi.org/10.2514/6.2025-1753

25. Hussien, H., and Saetti, U., "Analytical Linearization of a State-Space Viscous Vortex Particle Method for Rotary-Wing Simulations," Proceedings of the 81st Annual Forum of the Vertical Flight Society (VFS), May 2025. DOI: https://doi.org/10.4050/F-0081-2025-110

26. Griffiths, D., Ananthan, S., and Leishman, J., "Predictions of Rotor Performance in Ground Effect Using a Free-Vortex Wake Model," *Journal of the American Helicopter Society*, Vol. 50, Oct 2005, pp. 302–314. DOI: https://doi.org/10.4050/1.3092867

27. Maraniello, S., and Palacios, R., "State-Space Realizations and Internal Balancing in Potential-Flow Aerodynamics with Arbitrary Kinematics," *AIAA Journal*, Vol. 57, (6), 2019, pp. 2308–2321. DOI: https://doi.org/10.2514/1.J058153

28. Morino, L., and Kuot, C., “Subsonic Potential Aerodynamics for Complex Configurations: A General Theory,” *AIAA Journal*, Vol. 12, (2), 1974, pp. 191–197. DOI: https://doi.org/10.2514/3.49191

29. Katz, J., and Plotkin, A., *Low-Speed Aerodynamics*, Cambridge University Press, second edition, 2001. DOI: https://doi.org/10.1017/CBO9780511810329

30. Winckelmans, G. S., *Topics in vortex methods for the computation of three-and two-dimensional incompressible unsteady flows*, Ph.D. dissertation, California Institute of Technology, 1989. DOI: https://doi.org/10.7907/19HD-DF80

31. Celi, R., “State-Space Representation of Vortex Wakes by the Method of Lines,” *Journal of the American Helicopter Society*, Vol. 50, (2), Apr 2005, pp. 195–205. DOI: https://doi.org/10.4050/1.3092855

32. Zhu, W., Morandini, M., and Li, S., “Viscous Vortex Particle Method Coupling with Computational Structural Dynamics for Rotor Comprehensive Analysis,” *Applied Sciences*, Vol. 11, (7), 2021. DOI: https://doi.org/10.3390/app11073149

33. Melin, T., Isikveren, A., and Friswell, M., “Induced-Drag Compressibility Correction for Three-Dimensional Vortex-Lattice Methods,” *Journal of Aircraft - J AIRCRAFT*, Vol. 47, Jul 2010, pp. 1458–1460. DOI: https://doi.org/10.2514/1.C000197

34. Shah, M., “Development of Modified 3D Unsteady Vortex Panel Method,” , Aug 2018. DOI: https://doi.org/10.13140/RG.2.2.25966.54081

35. McDonald, R. A., and Ramos, A., “Constrained Hermite Interpolation for Mesh-Free Derivative Estimation Near and On Boundaries,” *AIAA Journal*, Vol. 49, (10), 2011, pp. 2248–2257. DOI: https://doi.org/10.2514/1.J051042

36. Light, J. S., “Tip Vortex Geometry of a Hovering Helicopter Rotor in Ground Effect,” *Journal of American Helicopter Society*, 1993, pp. 35–42.

37. Tan, J. F., Sun, Y. M., and Zhou, T. Y., “Simulation of the aerodynamic interaction between rotor and ground obstacle using vortex method,” *CEAS Aeronaut J*, Vol. 10, 2019, pp. 733–753. DOI: https://doi.org/10.1007/s13272-018-0346-8

38. Knight, M., and Hegner, R. A., “Analysis of Ground Effect on the Lifting Airscrew,” Technical report, NASA, 1941.

39. Saberi, H. A., and Maisel, M. D., “A Free-Wake Rotor Analysis Including Ground Effect,” American Helicopter Society 43rd Annual Forum Proceddings, St. Louis, MO, May 1987.

40. Rossow, V. J., “Effect of Ground and/or Ceiling Planes on Thrust of Rotors in Hover,” Technical report, NASA, 1985.

41. Saetti, U., and Horn, J. F., “Linear Time-Invariant Approximations of Nonlinear Time-Periodic Systems,” *Journal of the American Helicopter Society*, Vol. 68, Jan 2023. DOI: https://doi.org/10.4050/JAHS.68.012006

42. Lopez, M. J. S., and Prasad, J. V. R., “Linear Time Invariant Approximations of Linear Time Periodic Systems,” *Journal of the American Helicopter Society*, Vol. 62, (1), January 2017, pp. 1–10. DOI: https://doi.org/10.4050/JAHS.62.012006

43. Lopez, M., and Prasad, J., “Linear Time Invariant Approximations of Linear Time Periodic Systems,” *Journal of the American Helicopter Society*, Vol. 62, (1), Jan 2017, pp. 1–10. DOI: https://doi.org/10.4050/jahs.62.012006

44. Kokotovic, P. V., O’Malley, R. E., and Sannuti, P., “Singular Perturbations and Order Reduction in Control Theory, an Overview,” *Automatica*, Vol. 12, (2), 1976, pp. 123–132. DOI: https://doi.org/10.1016/0005-1098(76)90076-5

45. Howlett, J. J., “UH-60A Black Hawk Engineering Simulation Program. Volume 1: Mathematical Model,” Technical report, NASA-CR-166309, 1980.

46. Leishman, J. G., *Principles of Helicopter Aerodynamics*, Cambridge University Press, 2006. DOI: https://doi.org/10.1017/S0001924000087352

47. Borisov, E. A., “Experimental Research of Influence of Sites Size Restrictions on Aerodynamic Characteristics of the Rotor,” *Civil Aviation High Technologies*, Vol. 212, 2015, pp. 98–104.

48. Fradenburgh, E. A., “The Helicopter and the Ground Effect Machine,” *Journal of the American Helicopter Society*, Vol. 5, (4), Oct 1960, pp. 24–33. DOI: https://doi.org/10.4050/JAHS.5.4.24

49. Cheeseman, I. C., and Bennett, W. E., “The Effect of the Ground on a Helicopter Rotor in Forward Flight,” Technical Report ARC R&M 3021, Aeronautical Research Council, Available via Cranfield University’s Aerade Reports Archive, 1955.

50. Zhao, J., and He, C., “Physics-Based Modeling of Viscous Ground Effect for Rotorcraft Applications,” *Journal of American Helicopter Society*, 2015, pp. 1–13. DOI: https://doi.org/10.4050/F-0070-2014-9566

51. Kalra, T. S., Lakshminarayan, V. K., and Baeder, J. D., “CFD validation of micro hovering rotor in ground effect,” AHS International Specialists Conference Proceedings on Aeromechanics, San Francisco, CA, 2010.

52. Saetti, U., “Real-Time Simulation of a Shipborne Rotor via Linearized State-Space Free-Vortex Wake Models,” *Journal of Aircraft*, Vol. 61, (3), 2024. DOI: https://doi.org/10.2514/1.C037389

53. Xin, H., Prasad, J. V. R., and Peters, D. A., “Inflow model for simulation of helicopter flight in dynamic ground effect,” , 1999.

54. Rotaru, C., and Todorov, M., *Helicopter Flight Physics*, 02 2018. DOI: https://doi.org/10.5772/intechopen.71516

55. Tischler, M. B., and Remple, R. K., *Aircraft and Rotorcraft System Identification*, American Institute of Aeronautics and Astronautics, second edition, 2012. DOI: https://doi.org/10.2514/4.868207

56. Xin, H., Prasad, J., Peters, D., Itoga, N., Iboshi, N., and Nagashima, T., "Ground effect aerodynamics of lifting rotors hovering above inclined ground plane," 17th Applied Aerodynamics Conference, 1999.